General solution to reduce the point spread function effect in subpixel mapping

Qunming Wang [a, *], Chengyuan Zhang [a], Xiaohua Tong [a, *], Peter M. Atkinson [b,c,d]

[a] College of Surveying and Geo-Informatics, Tongji University, 1239 Siping Road, Shanghai 200092, China

[b] Faculty of Science and Technology, Lancaster University, Lancaster LA1 4YR, UK

[c] Geography and Environment, University of Southampton, Highfield, Southampton SO17 1BJ, UK

[d] Institute of Geographical Sciences and Natural Resources Research, Chinese Academy of Sciences, Datun Road, Beijing 100101, China

*Corresponding authors. E-mail: wqm11111@126.com (Q. Wang); xhtong@tongji.edu.cn (X. Tong)

Abstract: The point spread function (PSF) effect is ubiquitous in remote sensing images and imposes a fundamental uncertainty on subpixel mapping (SPM). The crucial PSF effect has been neglected in existing SPM methods. This paper proposes a general model to reduce the PSF effect in SPM. The model is applicable to any SPM methods treating spectral unmixing as pre-processing. To demonstrate the advantages of the new technique it was necessary to develop a new approach for accuracy assessment of SPM. To-date, accuracy assessment for SPM has been limited to subpixel classification accuracy, ignoring the performance of reproducing spatial structure in downscaling. In this paper, a new accuracy index is proposed which considers SPM performances in classification and restoration of spatial structure simultaneously. Experimental results show that by considering the PSF effect, more accurate SPM results were produced and small-sized patches and elongated features were restored more satisfactorily. Moreover, using the novel accuracy index, the quantitative evaluation was found to be more consistent with visual evaluation. This paper, thus, addresses directly two of the longest standing challenges in SPM (i.e., the limitations of the PSF effect and accuracy assessment undertaken only on a subpixel-by-subpixel basis).

Keywords: Remote sensing images, subpixel mapping (SPM), supper-resolution mapping, downscaling, spectral unmixing, point spread function (PSF), accuracy assessment.

1. Introduction

Land cover mapping is a common process in remote sensing in which land cover information is extracted from remotely sensed images. Mixed pixels, which generally contain more than one type of classes (Fisher, 1997), are a common phenomenon in remote sensing images. Conventional hard classification allocates each mixed pixel to a single land cover class. This can lead to the loss of a large amount of the latent land cover information in the observed images and is, thus, sub-optimal for land cover mapping. Spectral unmixing is a technique to estimate the class proportions at the original spatial resolution (hereafter, coarse proportions), but it fails to provide the spatial distribution of the land cover classes within each mixed pixel (i.e., at a scale finer than the original pixel). As a result, subpixel mapping (SPM) was developed for application to the coarse proportions estimated by spectral unmixing. SPM divides each coarse pixel into subpixels and assigns class labels to these subpixels, thus, providing more spatially detailed hard land cover information than conventional hard classification (Atkinson, 1997).

SPM is generally performed based on the assumption of spatial dependence, that is, spatially proximate observations are considered to be more likely to belong to the same class than more distant ones. Therefore, the objective of SPM can be characterized as the maximization of spatial dependence under the constraint that the coarse class proportions are honored. Over the past decades, various algorithms have been developed for SPM. In terms of the characterization of spatial dependence, SPM can be categorized mainly into two groups. One group describes the spatial relation between a subpixel and its neighboring pixels (i.e., subpixel-to-pixel-based methods), including subpixel/pixel spatial attraction model (SPSAM) (Mertens et al., 2006), area-to-point kriging (ATPK) (Wang et al., 2018), indicator co-kriging (ICK) (Jin et al., 2012), kriging (Verhoeye and De Wulf, 2002), back-propagation neural network (Wu et al., 2011), radial basis function (RBF) interpolation

(Wang et al., 2014a) and double-calculated spatial attraction model (DSAM) (Wu et al., 2018). The other group describes the spatial relation between a subpixel and its neighboring subpixels (i.e., subpixel-to-subpixel-based methods). Solutions in this group include pixel-swapping algorithm (PSA) (Atkinson, 2005), Hopfield neural network (HNN) (Tatem et al., 2001), genetic algorithm (Mertens et al., 2003) and maximum *a posteriori* (MAP) (Zhong et al., 2015). Moreover, some methods combine both types of spatial dependences (Chen et al., 2018a; Ling et al., 2014). In all these methods, although spatial dependence is described in different ways, SPM is applied to the output of spectral unmixing, namely, the coarse class proportions.

To circumvent the heavy dependence on the coarse proportions, SPM can be applied directly to the original coarse remote sensing images. Commonly used solutions are spatial-spectral models (e.g., Markov random field (MRF) (Chen et al., 2020; Li et al., 2014; Tolpekin and Stein, 2009)). These methods can reduce the uncertainty propagated from the coarse proportions to some extent. However, spatial-spectral models may not be beneficial for reproducing spatial structure information when relaxing the reliance on coarse proportions, as more emphasis is placed on the spatial part (always characterized by a local smoothness term) by assigning a larger weighting parameter. This process can produce over-smooth predictions, which can fail to reproduce small-sized patches and elongated features. Thus, appropriate weighting parameters need to be determined for spatial-spectral-based SPM. Moreover, the spatial part needs to be characterized more reasonably.

In recent years, SPM has also been extended from the conventional spatial domain to the spatial-temporal domain for time-series images and spatial-temporal SPM methods have been developed (Li et al., 2017; Zhang et al., 2017), which can make use of the temporal information in time-series images. In addition, learning-based SPM methods have been investigated which assume similarities in spatial structure between the target data and auxiliary training data (Chen et al., 2018b; Ling and Foody, 2019; Ma et al., 2019).

In existing spectral unmixing and SPM, it is assumed that each pixel consists solely of the signal within its scanning area (Kaiser and Schneider, 2008; Settle, 2005). However, the point spread function (PSF) effect exists ubiquitously in remote sensing images and influences the observed images greatly. The PSF effect originates from the physical, optical and electronic properties of sensors (Markham, 1985; Peng et al., 2015).

Mathematically, due to the PSF effect, the pixel value (e.g., reflectance, radiance, digital number, etc.) is a weighted convolution of contributions from both the observed pixel and its neighboring pixels. Such an effect leads to large errors in pixel values of both dark and bright areas. Specifically, the proportion value for dark targets surrounded by bright backgrounds is biased upwards, and the proportion value for bright targets surrounded by dark pixels is biased downwards. Therefore, the PSF effect constitutes an inherent source of uncertainty in each observed coarse pixel (Huang et al., 2002) and in all land cover mapping based on spectral unmixing and SPM.

In previous studies, the PSF effect was demonstrated to affect greatly the accuracy of the coarse proportions produced by spectral unmixing (Townshend et al., 2000; Wang et al., 2018). As a pre-processing step necessary for SPM, this inaccuracy in the coarse proportions will also affect the reliability of SPM directly. Specifically, in existing SPM methods, the PSF-contaminated coarse proportions are used as the 'coherence constraint' where the number of subpixels for each class is fixed accordingly. As a result, almost all existing SPM methods fail to account for the great impact of the inherent PSF. Wang and Atkinson (2017) proposed an optimization-based method to account for the PSF effect in the SPM process. This is one of the very few studies that considers the PSF effect in SPM. Specifically, a HNN model is constructed where the proportion constraint is characterized as the difference between the observed PSF-contaminated coarse proportion and the coarse proportion simulated by convolving the interim SPM realization with the PSF. The proportion constraint guides the optimization process and the optimal SPM solution is approached gradually. It was demonstrated that by considering the PSF effect, the HNN-based method can produce more accurate SPM predictions. However, the main limitation of HNN is that it fails to reproduce small-sized features. This is because the energy function of the HNN is characterized by a local smoothness term and a coherence constraint term, in which the constraint is always not strictly satisfied and the coarse proportions are not perfectly maintained based on the assumption of local smoothness during the optimization process. This is different from SPM methods that honour perfectly the coarse proportions. As a result, small-sized objects that produce

small proportions cannot be guaranteed to be represented by the HNN in most cases. Furthermore, the computational burden is heavy as a large number of iterations is required in the optimization process.

Different from the above-mentioned method that is developed based on a specific SPM model (e.g., HNN), in this paper, a general solution is proposed to reduce the PSF effect in SPM. The core idea of the solution is to consider the PSF effect in the pre-spectral unmixing process and provide enhanced coarse proportions for SPM (Wang et al., 2018). In this case, the determination of the number of subpixels for each class within each coarse pixel in the post-SPM process is guided by the enhanced coarse proportions. Hence, the proposed model based on the enhanced coarse proportions is suitable for any existing SPM methods that use spectral unmixing as a pre-processing step, including both the subpixel-to-pixel and subpixel-to-subpixel classes of method mentioned earlier. The advantage of the general solution is that it can restore satisfactorily small-sized patches while consuming less time. In this paper, both the subpixel-to-pixel (i.e., ATPK) and the subpixel-to-subpixel (i.e., PSA) method classes are extended to account for the PSF effect.

As acknowledged widely, SPM is essentially a hard classification technique performed at a finer spatial resolution than the original data. Quantitative assessment of the accuracy of SPM based on classification at the level of the smallest unit (i.e., subpixel) is accepted as valuable (Foody, 2002). However, SPM is also a downscaling technique involving transformation of spatial scale (Ge et al., 2019). Therefore, the accuracy assessment applied to the results of SPM should concern not only the per-subpixel performance of the classification, but also the ability to recover interesting spatial structure features and boundary information after downscaling. In recent years, increasing attention has been paid to the ability to reproduce finer resolution spatial structure information in land cover using SPM. For example, Ling et al. (2012) extracted rectangular building objects at a finer spatial resolution conditional upon prior shape information. Moreover, Atkinson (2004) used the two-point histogram to characterize spatial pattern, and the optimal SPM prediction was assumed to be the one that was most similar in spatial structure to that of the available training image. To the best of our knowledge, however, existing accuracy evaluation of SPM is based universally on subpixel classification accuracy, neglecting the accuracy of reproducing spatial structure. Therefore, there is a great

need for a new accuracy index that can account for the accuracies of subpixel classification and spatial structure reproduction simultaneously for SPM.

To fill the need mentioned above, as another contribution in this paper, a new accuracy index for more comprehensive evaluation of SPM is proposed which evaluates the restoration of spatial structure in addition to conventional classification-based indices (e.g., producers' accuracy (PA), users' accuracy (UA) and overall accuracy (OA). The semivariogram has been used widely to quantify the spatial variation in land cover (Curran, 1988). It is used to characterize the spatial structure in the land cover class map predicted by SPM in this paper. The accuracy of the semivariogram can be quantified straightforwardly to represent the accuracy of restoring spatial pattern. On this basis, an integrated error index is proposed coupled with a conventional classification-based index.

The main contributions of this paper are, thus, twofold.

1) A general solution is proposed to reduce the influence of the PSF in SPM and to produce more reliable subpixel land cover maps. The PSF effect has seldom been considered in SPM and the reliability of the predicted subpixel maps is affected greatly. The proposed model provides a completely new insight to reduce the PSF effect. It is suitable for *any* existing SPM methods using spectral unmixing predictions as input. Moreover, it can reproduce small-sized and elongated features and is computationally fast.
2) A new error index is developed for more objective quantitative evaluation of SPM prediction. Accuracy assessment for SPM is a long standing issue (Atkinson, 2009). It is crucial to evaluate the performance of both the classification and downscaling (i.e., spatial structure reproduction) aspects of SPM. Along with conventional classification accuracy-based evaluation, the proposed error index uses the semivariogram to assess the accuracy of spatial structure reproduction simultaneously. This paper, thus, provides a first step towards more comprehensive, integrated accuracy assessment for SPM.

The remainder of this paper is divided into four sections. The second section first introduces the mechanism of the proposed general solution for considering the PSF effect in SPM. The extended versions of two types of SPM methods are then introduced in Section 2.2, followed by details of the proposed error index in Section 2.3.

149 The third section provides the experimental results for three datasets to demonstrate the effectiveness of the
150 proposed SPM method and the proposed accuracy index. Section 4 discusses open issues in the proposed
151 general SPM method and the new accuracy index, followed by a conclusion in Section 5.
152
153 **2. Methods**
154
155 *2.1. The proposed general SPM model considering the PSF effect*
156 As a post-processing technique of spectral unmixing, SPM uses the coarse proportion data predicted from
157 spectral unmixing as input. Therefore, the coarse proportions play an important role in SPM. In existing SPM
158 methods, the coarse proportions are assumed not to be influenced by the PSF effect (Wang et al., 2018). As
159 depicted by Wang and Atkinson (2017), however, the PSF effect is ubiquitous in reality and influences greatly
160 the spectral unmixing results. To provide more reliable input and enhance SPM, it is important to reduce the
161 influence of the PSF effect in the pre-processing spectral unmixing.
162 Based on this idea, in this paper, a general model that is suitable for *any* SPM methods using spectral
163 unmixing predictions as input is proposed to reduce the impact of the PSF on SPM. Specifically, the ideal
164 coarse proportions not contaminated by the PSF effect are estimated by a downscale-then-upscale process, as
165 shown in Fig. 1. The principles are introduced explicitly below.
166 Suppose $F_k(v)$ is the ideal fine spatial resolution proportion (hereafter, fine proportion) for class k (k=1,
167 2, …, K, where K is the number of land cover classes) in subpixel v located within coarse pixel V. The ideal
168 fine proportions are not contaminated by the PSF effect. The coarse proportions $F_k(V)$ for class k predicted
169 from spectral unmixing can be described as a convolution of the ideal fine proportions (Wang et al., 2018)

$$F_k(V) = F_k(v) * h_V \tag{1}$$

171 where * is the convolution operator and h_V is the PSF filter.
172 In the existing literature on spectral unmixing, the coarse proportions in a pixel are assumed to be the

average of the fine proportions of all subpixels located within the coarse pixel (i.e., a non-PSF or an ideal square wave filter h'_V is assumed). In reality, however, the actual PSF h_V is distinctly different from the ideal h'_V, and h_V is commonly assumed to be a Gaussian PSF (Van der Meer, 2012, Wang et al., 2018). The Gaussian filter can characterize appropriately the influence of neighboring subpixels on the coarse proportions of the center pixel: subpixels closer to the center of the pixel hold greater weight, and more importantly, the spatial coverage the of PSF is generally larger than a coarse pixel (i.e., not only the subpixels falling in the center coarse pixel, but also neighboring subpixels that contribute to the coarse proportions of the center pixel).

According to Eq. (1), once the PSF is known, the ideal fine proportion $F_k(v)$ can be predicted from the PSF-contaminated spectral unmixing prediction $F_k(V)$. This process is essentially downscaling. To solve the inverse problem by downscaling, the key is to account for the PSF and more precisely, the contributions of neighboring pixels to the coarse proportions of the center pixel. As a powerful method for downscaling, the ATPK method can achieve this by relating the semivariogram at different scales using the PSF. It is, thus, adopted to estimate each fine proportion in this paper. Specifically, the ATPK-derived fine proportion is calculated as a linear weighted sum of the coarse proportions in neighboring pixels as follows:

$$\hat{F}_k(v) = \sum_{j=1}^{N} \lambda_j F_k(V_j) \tag{2}$$

where λ_j is the weight for neighboring coarse pixel V_j and N is the number of neighboring pixels. The weights λ_j (j=1, 2, …, N) are calculated based on a kriging matrix composed of semivariograms at different spatial resolutions. More details can be found in Kyriakidis (2004).

Notably, when solving the downscaling problem under the PSF effect in Eq. (2), the condition (i.e., constraint) in Eq. (1) needs to be satisfied. The ATPK method holds the advantage that once the predictions $\hat{F}_k(v)$ are convolved with the PSF h_V, the original coarse proportions will be reproduced exactly, that is, Eq. (1) is strictly satisfied (Kyriakidis, 2004)

$$\hat{F}_k(v) * h_V = F_k(V). \tag{3}$$

Therefore, $\hat{F}_k(v)$ is considered to be a reliable solution to the ideal fine proportion identified in Eq. (1). After the ideal fine proportions are predicted, they can be convolved with the ideal square wave filter h'_V to estimate the coarse proportion $T_k(V)$ not contaminated by the PSF effect

$$\hat{T}_k(V)=\hat{F}_k(v)*h'_V. \tag{4}$$

More precisely, based on the definition of h'_V, the enhanced coarse proportion for class *k* can be further simplified as the average of fine proportions $\hat{F}_k(v)$ in subpixels located in V_j. That is, for each pixel V_j, we have

$$\hat{T}_k(V_j)=\frac{1}{s^2}\sum_{i=1}^{s^2}\hat{F}_k(v_{i,j}). \tag{5}$$

where $v_{i,j}$ are the subpixels within the coarse pixel V_j. Before the enhanced coarse proportion $\hat{T}_k(V)$ is used for post-SPM, it needs to be further normalized so that the sum of proportions of all classes in each pixel is equal to one.

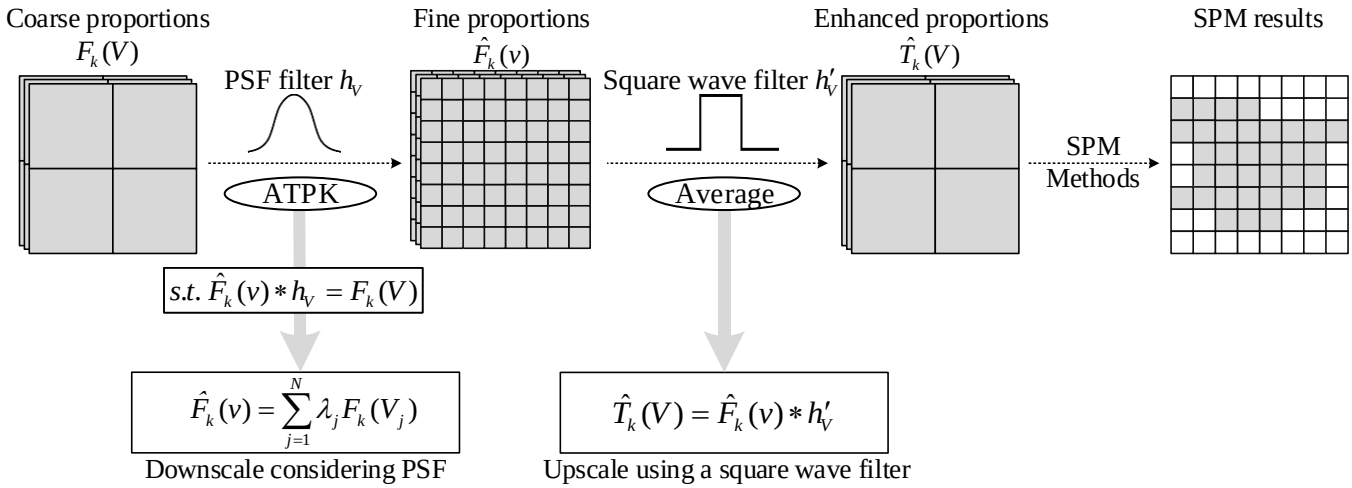

Fig. 1. Systemic framework of SPM methods considering the PSF effect.

2.2. SPM based on the general model

Based on the goal of maximizing spatial dependence, SPM methods can be divided into two main types. One is based on the spatial dependence between a subpixel and its neighboring subpixels, while the other is based on the spatial dependence between a subpixel and its neighboring coarse pixels. The goal of both methods can be quantified as maximizing an objective function characterizing spatial dependence. Specifically, for each coarse pixel V_j in the coarse image containing *K* land cover classes, the mathematical model of the goal is

$$\begin{aligned} &\max\ G_j = \sum_{k=1}^{K}\sum_{i=1}^{s^2} D_k(v_{i,j}) I_k(v_{i,j}) \\ &s.t.\ \sum_{k=1}^{K} I_k(v_{i,j}) = 1,\ i = 1,2,...,s^2 \\ &\sum_{i=1}^{s^2} I_k(v_{i,j}) = \hat{T}_k(V_j) \bullet s^2,\ k = 1,2,...,K \end{aligned} \tag{6}$$

where G_j is the objective function, $v_{i,j}$ is a subpixel located in coarse pixel V_j and $D_k(v_{i,j})$ is the quantified spatial dependence of subpixel $v_{i,j}$ for class *k*. $I_k(v_{i,j})$ is a class indicator defined as follows

$$I_k(v_{i,j}) = \begin{cases} 1, \text{ if subpixel } v_{i,j} \text{ belongs to class } k \\ 0, \text{ otherwise.} \end{cases}. \tag{7}$$

The two constraints in Eq. (6) mean that each subpixel is assigned to only one class and the subpixels for each class (e.g., class *k*) need to satisfy the coherence constraint provided by the coarse proportion (e.g., $\hat{T}_k(V)$).

It is clear that once the enhanced coarse proportion $\hat{T}_k(V)$ is predicted, it can be used for any SPM methods that use it as input, including both subpixel-to-subpixel-based and subpixel-to-pixel-based methods. The adaptation of the two groups of methods to the enhanced coarse proportions is introduced below.

1) Subpixel-to-pixel methods considering the PSF effect: For the subpixel-to-pixel class of SPM methods, $D_k(v_{i,j})$ in Eq. (6) is described explicitly as

$$D_k^{SP}(v_{i,j}) = \sum_{n=1}^{N_{SP}} \omega_{SP}(v_{i,j}, V_n) \hat{T}_k(V_n) \tag{8}$$

where V_n is the coarse neighbor of subpixel $v_{i,j}$ and a window size of 5×5 coarse pixels were considered in this

paper. N_{SP} is the number of neighboring coarse pixels. Additionally, $\omega_{SP}(v_{i,j}, V_n)$ is a distance-dependent weight function for the dependence between subpixel $v_{i,j}$ and neighboring pixel V_n.

For the subpixel-to-pixel class of methods, $D_k^{SP}(v_{i,j})$ calculated in Eq. (8) is the soft class value for each subpixel and takes a value between 0 and 1. The final subpixel class is determined using a class allocation method, based on the rank of the estimated soft class values and proportion constraint. This group of SPM methods is also termed soft-then-hard SPM (STHSPM) in Wang et al. (2014b). The methods falling into this group include bilinear or bicubic interpolation, SPSAM, ATPK and ICK. These methods hold the advantage of small computational cost. In this paper, the class allocation is performed in units of class (i.e., the UOC method in Wang et al. (2014b)).

2) Subpixel-to-subpixel methods considering the PSF effect: For the subpixel-to-subpixel class of SPM methods, $D_k(v_i)$ in Eq. (6) is described as

$$D_k^{ss}(v_{i,j}) = \sum_{n=1}^{N_{SS}} \omega_{SS}(v_{i,j}, v_n) I_k(v_n) \tag{9}$$

where v_n is the neighboring subpixel of $v_{i,j}$ and a window size of 5×5 subpixels were used in this paper. $I_k(v_n)$ has the same meaning as in Eq. (7). In addition, $\omega_{SS}(v_{i,j}, v_n)$ is a distance-based weight function for the dependence between subpixel $v_{i,j}$ and neighboring subpixel v_n. Accordingly, the sum of $D_k^{ss}(v_{i,j})$ multiplied by the class indicator is maximized to obtain the optimal SPM result under the constraint conditions in Eq. (6).

This class of method requires a number of iterations to approach the optimal solution. Common choices for this type of SPM method are PSA, genetic algorithm and HNN. These methods can recover small targets, but generally take a relatively long time for optimization.

2.3. The proposed index for evaluation of SPM accuracy

For quantitative assessment of SPM, the existing classification-based evaluation schemes (e.g., PA, UA and OA) have been used widely, as SPM is essentially a hard classification technique. However, it is known that

SPM is also a downscaling technique that reproduces land cover information at a finer spatial resolution than the observed images. For this scale change process, we should also be concerned about the reproduction of the spatial structure information in land cover, including the shape of objects and the spatial pattern of each land cover class. Classification-based evaluation methods evaluate classification accuracy on the basis only per-pixel or, in the SPM case, per-subpixel and fail to account for spatial structure. An example is provided in Fig. 2 to illustrate this issue. Suppose a coarse pixel covers a gray target and white background (Fig. 2(a)). Three possible predictions for the two classes are shown in Fig. 2(b)-(d). All per-subpixel classification accuracies (including PA, UA and OA) are larger for Fig. 2(b) than for Fig. 2(d). However, the reproduction of the spatial structure (i.e., linear feature) in Fig. 2(d) is obviously closer to the reference than in Fig. 2(b). For some SPM methods that are not completely slavish to the coarse proportions (e.g., HNN) the prediction, as shown in Fig. 2(c), also produces larger accuracies than that in Fig. 2(d). Thus, it is necessary to use a more suitable index for objective quantitative evaluation of SPM.

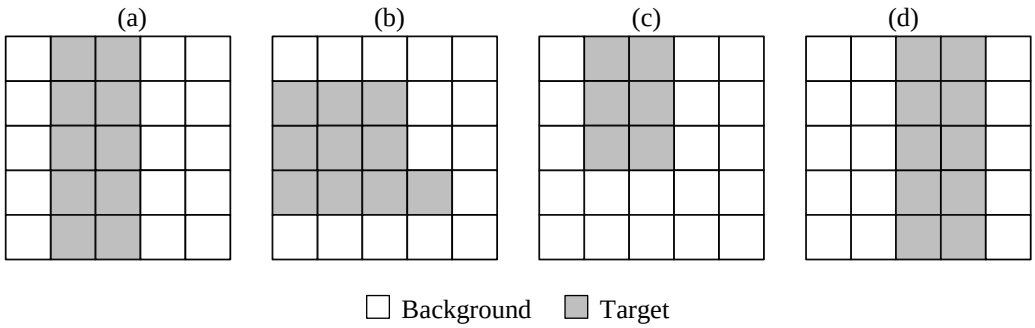

Fig. 2. A schematic example illustrating the limitations of using only classification-based indices for evaluation of SPM. (a) Reference land cover map. (b) Prediction 1 where OA=17/25 and PA=UA=6/10 for target. (c) Prediction 2 where OA=21/25 and PA=6/10, UA=1 for target. (d) Prediction 3 where OA=15/25 and PA=UA=5/10 for target.

1) Error of semivariogram: The semivariogram is widely acknowledged to be able to reflect the spatial structure of land cover classes (Curran, 1988). It is proposed to evaluate quantitatively the accuracy of reproducing spatial structure using SPM in this paper. The semivariogram is calculated on a subpixel scale binary land cover map of each class. For class k, the semivariagram at lag $\mathbf{h}$ is calculated as

$$\gamma_k(\mathbf{h}) = \frac{1}{2N(\mathbf{h})} \sum_{i=1}^{N(\mathbf{h})} [I_k(v_{\mathbf{x}_i}) - I_k(v_{\mathbf{x}_i+\mathbf{h}})]^2 \quad (10)$$

where $N(\mathbf{h})$ is the number of paired pixels at lag $\mathbf{h}$, $\mathbf{x}_i$ and $\mathbf{x}_i + \mathbf{h}$ are the locations of $v_{\mathbf{x}_i}$ and $v_{\mathbf{x}_i+\mathbf{h}}$, and $I_k(v_{\mathbf{x}_i})$ and $I_k(v_{\mathbf{x}_i+\mathbf{h}})$ have the same meaning as in Eq. (7).

Large $\gamma_k(\mathbf{h})$ indicates that the difference between the paired pixels at lag $\mathbf{h}$ for class *k* is large (i.e., a large spatial variance). Therefore, the semivariograms characterise the nature of the spatial dependence, and do this per land cover class (Balaguer-Beser et al., 2013; Curran, 1988). In this way, the semivariogram is a suitable function to assess the (dis)similarity of spatial structure between different images. The mean absolute error (MAE) is a common choice to quantify the difference between data and it is used to evaluate the 'error' of the semivariogram (i.e., the difference between semivariograms of the SPM predictions and the reference) in this paper.

2) The proposed integrated error (IE) index: As mentioned earlier, SPM has two characteristics, that is, classification and downscaling. Thus, it is desirable to develop an index that can reflect the accuracy in both parts. Suppose PA_k represents the PA of class *k* in the SPM results (i.e., subpixel classification accuracy). In our proposed integrated error index (IE_k), PA_k of classification and *MAE* of semivariogram are considered simultaneously to fully evaluate the SPM accuracy, expressed as

$$IE_k = (1 - PA_k)^{\alpha} \times MAE_k{}^{\beta} \quad (11)$$

where α and β are two parameters controlling the contributions of pixel classification and spatial structure recovery accuracies. In this paper, for simplicity, both parameters are set to 1, and then the proposed new index IE_k can be simplified as

$$IE_k = (1 - PA_k) \times MAE_k. \quad (12)$$

297 As seen in Eq. (12), the proposed index IE_k evaluates the error of SPM results for each land cover class in
298 terms of both subpixel prediction accuracy (i.e., by $1-PA_k$) and spatial structure prediction accuracy (i.e., by
299 MAE_k of semivariograms). The larger the value, the smaller the accuracy of SPM.
300
301 **3. Experiments**
302
303 To demonstrate the effectiveness of the proposed SPM approach in reducing the PSF effect as well as the
304 new index for accuracy assessment, experiments on four datasets were implemented. To evaluate the method
305 objectively, the reference fine spatial resolution land cover maps need to be known perfectly. Therefore, for the
306 first three datasets, simulated coarse resolution data were used, which can also help to concentrate solely on the
307 performance of SPM (Atkinson, 2009). Specifically, the available land cover map was degraded with a PSF to
308 simulate coarse proportions contaminated by the PSF effect. To further account for the greater uncertainty in
309 real spectral unmixing processes (i.e., for real data), for the fourth dataset a simulated coarse multispectral
310 image was used to examine the performance of SPM. The widely used Gaussian PSF was considered in the
311 experiments. The width of the PSF was set to half of the coarse pixel size. Two zoom factors *s* were tested: 4
312 and 8. For example, *s*=4 means that each 4×4 subpixels are aggregated to a coarse pixel when simulating the
313 coarse data and each coarse pixel is devided into 4×4 subpixels in SPM.
314 As mentioned earlier, the proposed general SPM model for considering the PSF is shown theoretically to be
315 suitable for any SPM methods using spectral unmixing as pre-processing. To validate the generalization ability
316 of the proposed model for reducing the effect of PSF on SPM, the two typical families of methods based on
317 different spatial dependencies (as introduced in Section 2.2) were implemented. Specifically, considering their
318 encouraging performances demonstrated in the literature, the ATPK and PSA methods were used for the
319 subpixel-to-pixel and subpixel-to-subpixel cases, respectively. To validate the benefit of considering the PSF
320 effect, SPM based on the enhanced coarse proportions and the original PSF-contaminated coarse proportions
321 (i.e., without considering the PSF effect) were compared. Moreover, the recently developed HNN method

accounting for the PSF effect (Wang and Atkinson, 2017) was also used as a benchmark method. In summary, five methods were tested, namely, HNN-with-PSF, PSA-without-PSF, PSA-with-PSF, ATPK-without-PSF and ATPK-with-PSF, where "with-PSF" means SPM was performed on the enhanced proportions (i.e., the PSF effect is considered), while "without-PSF" means SPM was performed on the original PSF-contaminated proportions.

The first three datasets are from the National Land Cover Database 2001 (NCLD 2001), as shown in Fig. 3. Each land cover map has a size of 496×496 pixels. The first map covers an area in Ohio, the second an area in South Carolina and the third an area in California. Four classes are presented in the three maps, namely, water, urban, agriculture and forest. The last dataset is a Landsat 7 Enhanced Thematic Mapper plus (ETM+) image acquired in August 2001 which covers farmland in the Liaoning Province, China, again with four land cover classes (marked as C1-C4). The spatial extent is 240×240 Landsat pixels.

3.1. Proportion results

The proposed model accounts for the PSF effect in the pre-processing spectral unmixing and enhances the original coarse proportions. Thus, it is critical to evaluate the coarse proportions before and after the consideration of the PSF effect. For objective assessment, the land cover map was degraded by a square wave filter to produce reference coarse proportions.

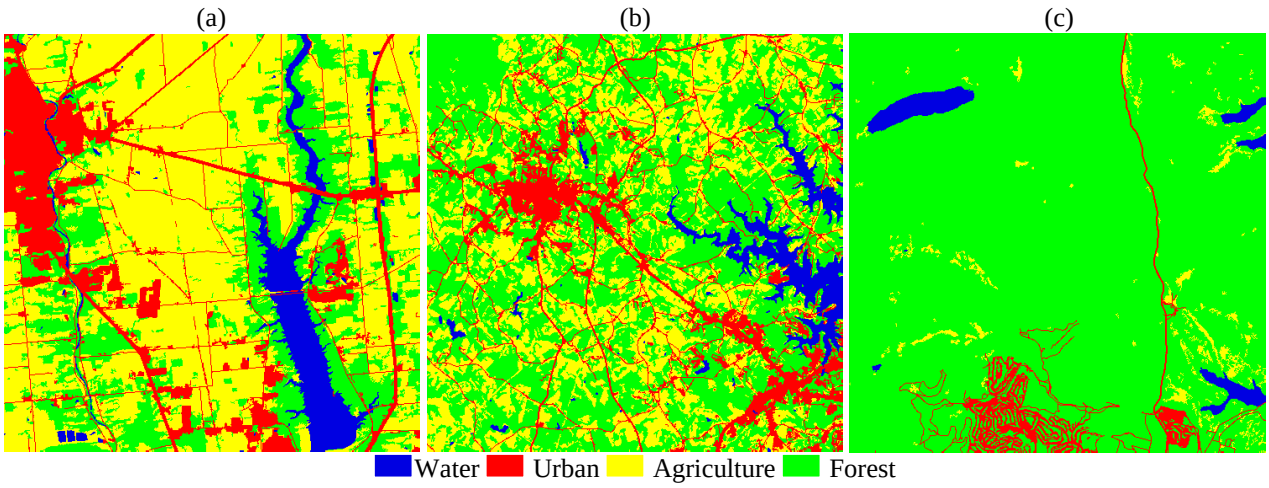

Fig. 3. The 30 m land cover maps (496×496 pixels) used in the experiments. (a) Ohio. (b) South Carolina. (c) California.

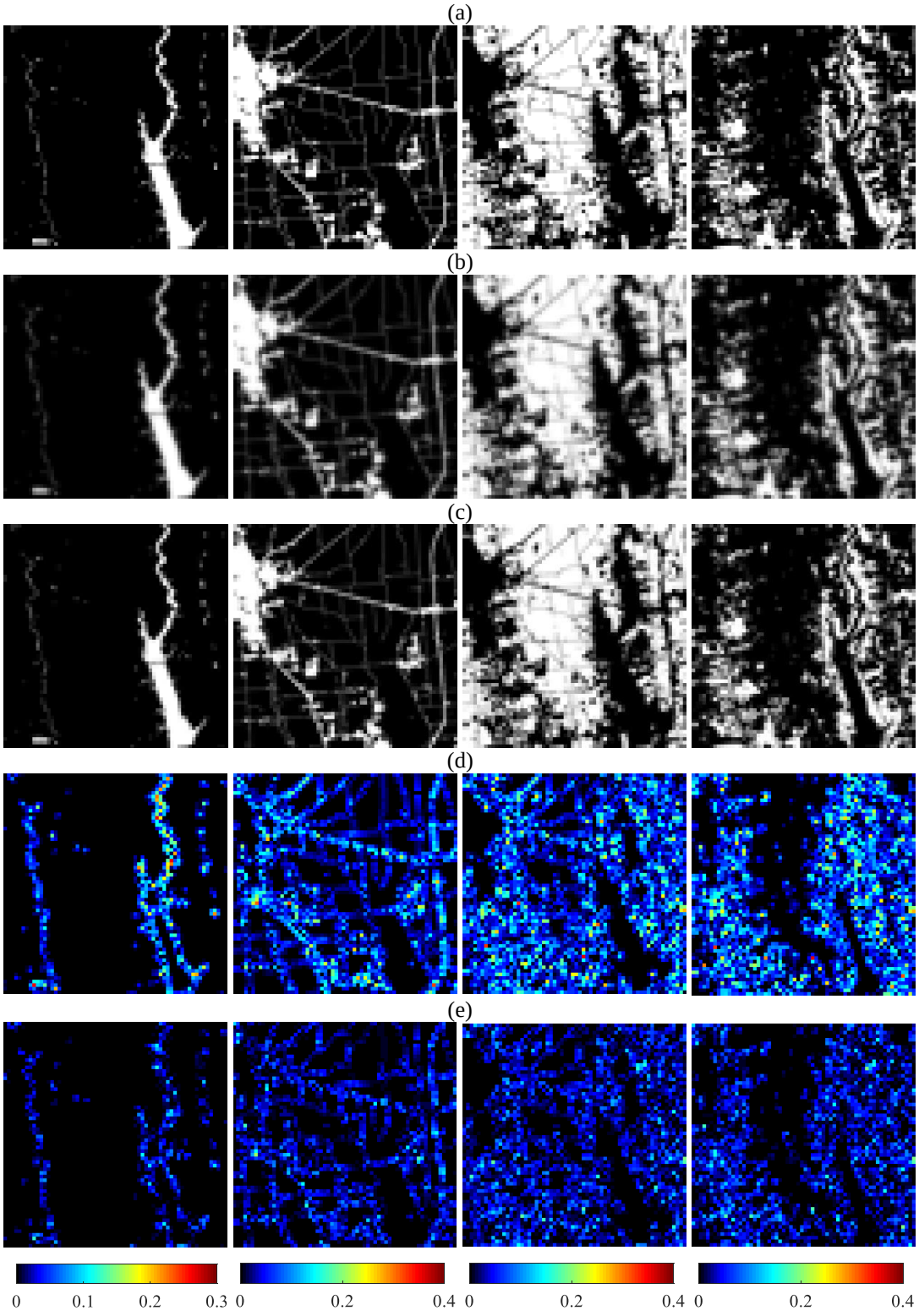

Fig. 4. 240 m coarse proportion images of Ohio (s=8, 62×62 pixels). (a) Reference produced by convolving the 30 m land cover map in Fig. 3(a) with an ideal wave square PSF. (b) PSF-contaminated proportion images produced by convolving Fig. 3(a) with a Gaussian PSF. (c) Enhanced proportion images produced by reducing the PSF effect in spectral unmixing. (d) Absolute value of proportion error between the PSF-contaminated proportion image and the reference. (e) Absolute value of proportion error between the enhanced proportion image and the reference. From left to right are the results for water, urban, agriculture and forest.

Fig. 4 shows the 240 m coarse propotion images for each class for the Ohio dataset. Fig. 4(a) shows the ideal coarse propotions without the PSF effect (i.e., degrading Fig. 3(a) using a 8×8 square wave PSF). The proportion images contaminated by the Gaussian PSF are displayed in Fig. 4(b). Fig. 4(c) shows the enhanced coarse proportions produced by the proposed ATPK-based downscale-then-upscale method. Due to the negative impact of the PSF effect, Fig. 4(b) is obviously ambiguous. Compared to Fig. 4(b), the images in Fig. 4(c) are much brighter and visually closer to the reference in Fig. 4(a). For clearer comparison between Fig. 4(b) and Fig. 4(c), the absolute value of the proportion errors (i.e., compared to the reference) of the two types of proportions are shown in Fig. 4(d) and Fig. 4(e). The error images in Fig. 4(d) are much darker than Fig. 4(e), suggesting that the proportion error is reduced obviously in the enhanced proportions. Specifically, in most cases, the proportion errors in Fig. 4(d) are close to 0.2 while those in Fig. 4(e) are less than 0.1.

Table 1 Quantitative assessment (in terms of RMSE and CC) on each land cover class for the three datasets

			RMSE		CC	
		Class	Original proportion	Enhanced proportion	Original proportion	Enhanced proportion
Ohio	s=4	Water	0.0267	**0.0130**	0.9935	**0.9984**
		Urban	0.0560	**0.0323**	0.9853	**0.9948**
		Agriculture	0.0709	**0.0390**	0.9875	**0.9961**
		Forest	0.0674	**0.0350**	0.9842	**0.9954**
	s=8	Water	0.0312	**0.0134**	0.9905	**0.9981**
		Urban	0.0553	**0.0309**	0.9827	**0.9942**
		Agriculture	0.0722	**0.0383**	0.9850	**0.9955**
		Forest	0.0735	**0.0374**	0.9770	**0.9934**
South Carolina	s=4	Water	0.0307	**0.0139**	0.9885	**0.9975**
		Urban	0.0609	**0.0331**	0.9748	**0.9920**
		Agriculture	0.0882	**0.0452**	0.9713	**0.9914**
		Forest	0.0945	**0.0467**	0.9745	**0.9928**
	s=8	Water	0.0342	**0.0176**	0.9829	**0.9951**
		Urban	0.0544	**0.0296**	0.9735	**0.9913**
		Agriculture	0.0815	**0.0453**	0.9635	**0.9869**
		Forest	0.0928	**0.0499**	0.9644	**0.9877**
California	s=4	Water	0.0146	**0.0057**	0.9953	**0.9992**
		Urban	0.0313	**0.0193**	0.9787	**0.9916**
		Agriculture	0.0291	**0.0152**	0.9698	**0.9903**
		Forest	0.0443	**0.0250**	0.9817	**0.9938**
	s=8	Water	0.0210	**0.0079**	0.9900	**0.9984**
		Urban	0.0240	**0.0155**	0.9849	**0.9934**
		Agriculture	0.0270	**0.0139**	0.9629	**0.9880**
		Forest	0.0401	**0.0214**	0.9822	**0.9944**

In Table 1, the root mean square error (RMSE) and CC were listed for quantitative evaluation between the predicted proportions (i.e., original proportions contaminated by the PSF or enhanced proportions) and real proportions for all three datasets. Two degradation factors (s=4 and 8) were used to simulate the coarse proportions. As shown in Table 1, by considering the PSF effect, the RMSEs of the enhanced proportions are much smaller than those of the original PSF-contaminated proportions in all cases. More precisely, the RMSEs of the enhanced proportions are reduced by around 0.01 to 0.05. Meanwhile, the CCs of the enhaced proportions are larger than those for the original PSF-contaminated results. Specifically, the increase in CC by considering the PSF effect ranges from 0.005 to 0.025. Thus, the errors in the coarse proportions are reduced obviously by considering the PSF effect.

3.2. Qualitative evaluation on SPM results

The five methods (HNN-with-PSF, PSA-without-PSF, PSA-with-PSF, ATPK-without-PSF and ATPK-with-PSF) were applied based on the input enhanced or original coarse proportions. Figs. 5-7 display the SPM results (s=4) of the five methods for the three datasets. Moreover, the hard classification (HC) results based on the original coarse proportion images (i.e., HC-without-PSF) and enhanced coarse proportion images (i.e., HC-with-PSF) were provided. By HC, the classes of all subpixels in each coarse pixel are determined as the class with the maximum proportion.

Obviously, the boundaries of each class in the HC results are jagged and some elongated features smaller than a coarse pixel are eliminated completely; see Fig. 5(b1), Fig. 5(c1), Fig. 6(b1), Fig. 6(c1), Fig. 7(b1) and Fig. 7(c1). Compared to the HC results, the SPM methods produce more detailed, continuous and visually pleasing boundaries. In the five SPM results, without considering the PSF effect, the resulting maps of PSA-without-PSF and ATPK-without-PSF contain many sporadic artifacts, presenting noisy pixels around class boundaries. Furthermore, the urban class is scattered into several patches, which actually is a linear feature in the reference map, as shown in Fig. 5(e1), Fig. 5(g1), Fig. 6(e1) and Fig. 6(g1). Compared to the results of ATPK and PSA without considering the PSF, ATPK-with-PSF and PSA-with-PSF produce more

399 continuous results and the class boundaries are smoother and closer to the reference maps, see Fig. 5(f1), Fig.
400 5(h1), Fig. 6(f1) and Fig. 6(h1). It should be noted, however, that the elongated roads are incorrectly merged by
401 PSA. The reason is that PSA tends to aggregate small-sized patches when maximizing the spatial dependence
402 within the coarse pixel. With respect to the HNN-with-PSF method, it produces over-smooth results, especially
403 for the urban and agriculture classes, see Fig. 5(d), Fig. 6(d) and Fig. 7(d).
404
405

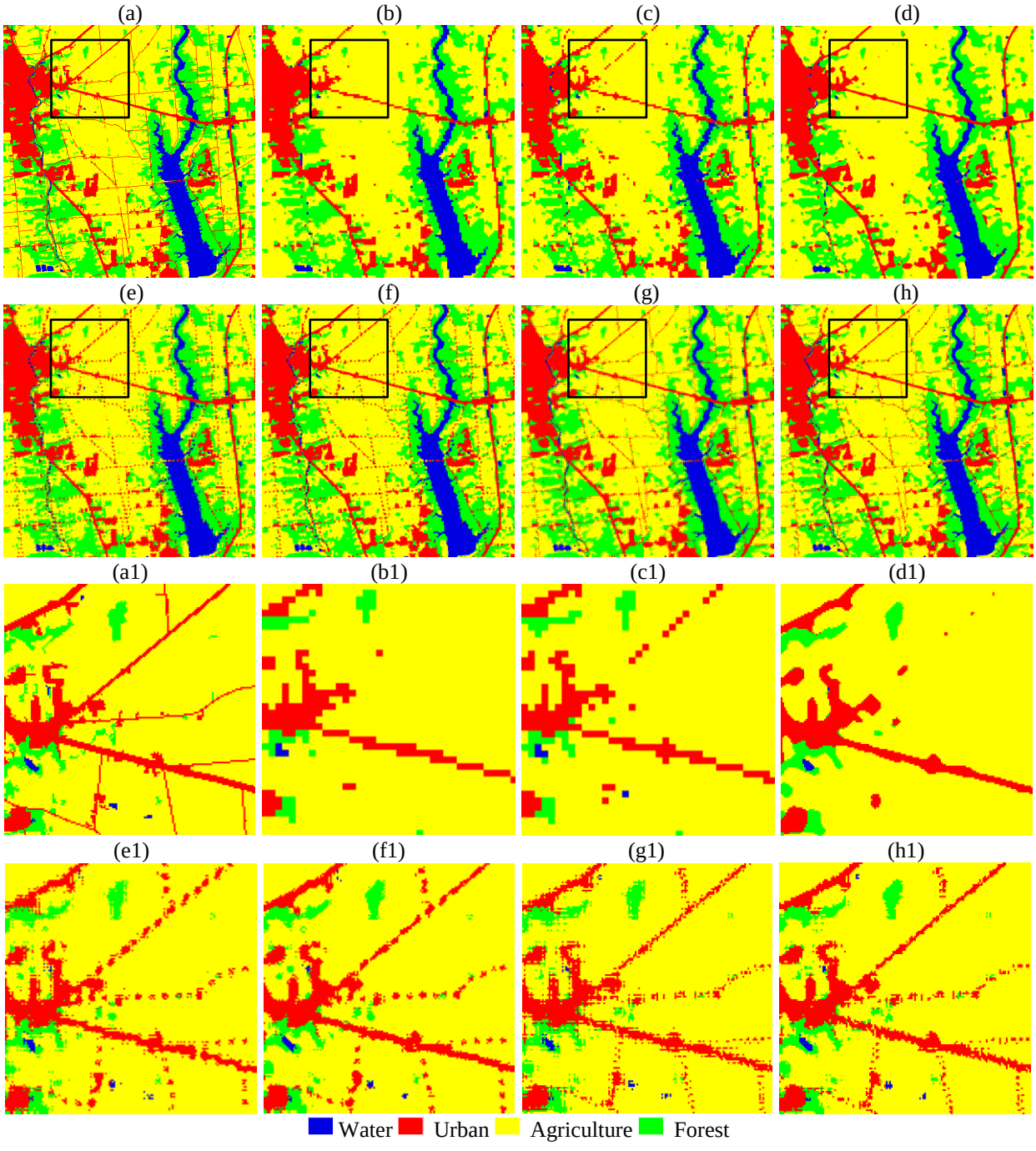

406
407
408
409
410
411
412
413

Fig. 5. The SPM results for the Ohio dataset with a zoom factor of 4 (496×496 pixels). (a) Reference. (b) HC-without-PSF. (c) HC-with-PSF. (d) HNN-with-PSF (Gaussian PSF). (e) PSA-without-PSF (i.e., with ideal square PSF). (f) PSA-with-PSF (Gaussian PSF). (g) ATPK-without-PSF (i.e., with ideal square PSF). (h) ATPK-with-PSF (Gaussian PSF). (a1)-(h1) Zoomed subareas of (a)-(h).

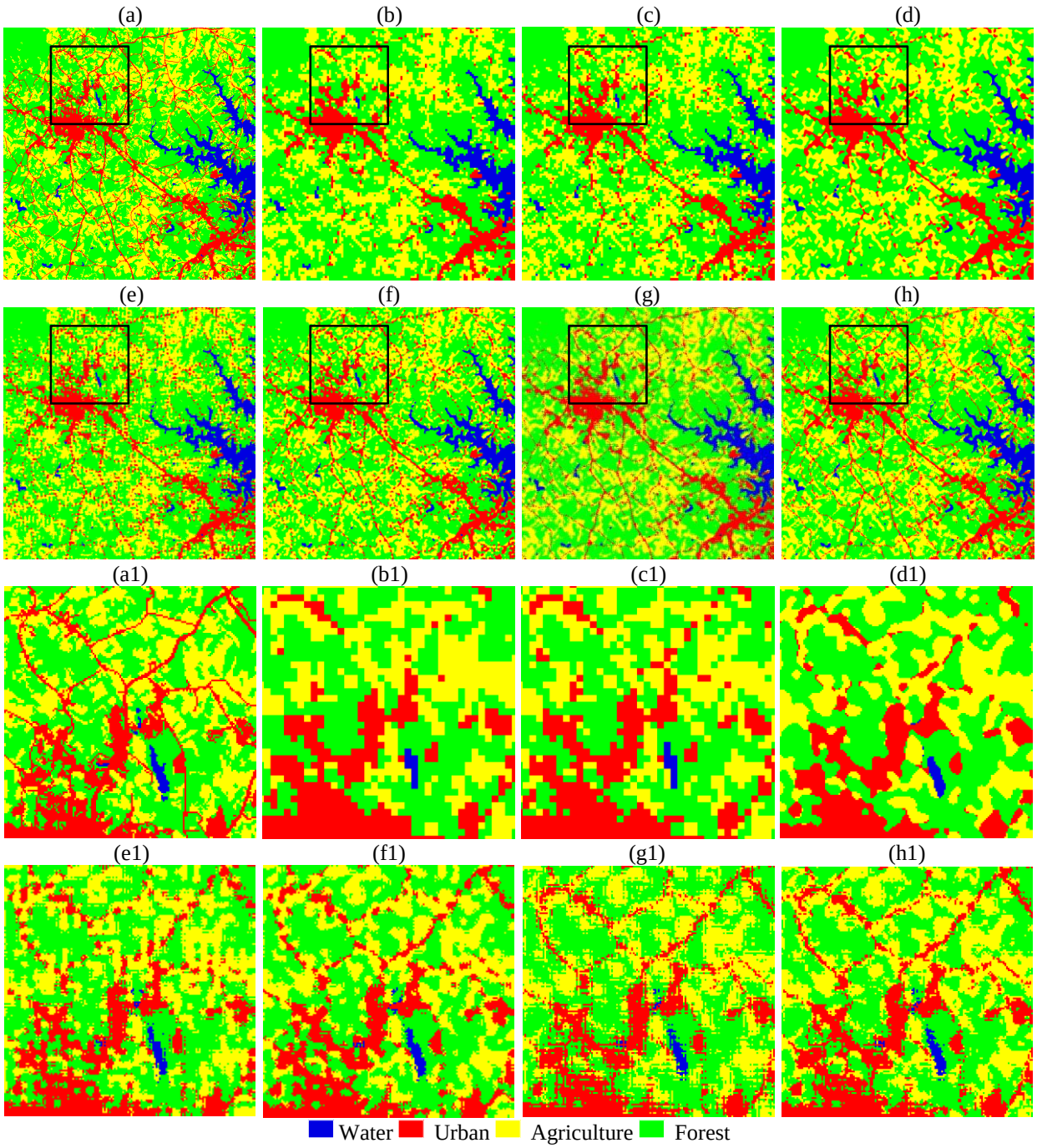

Fig. 6. The SPM results for the South Carolina dataset with a zoom factor of 4 (496×496 pixels). (a) Reference. (b) HC-without-PSF. (c) HC-with-PSF. (d) HNN-with-PSF (Gaussian PSF). (e) PSA-without-PSF (i.e., with ideal square PSF). (f) PSA-with-PSF

(Gaussian PSF). (g) ATPK-without-PSF (i.e., with ideal square PSF). (h) ATPK-with-PSF (Gaussian PSF). (a1)-(h1) Zoomed subareas of (a)-(h).

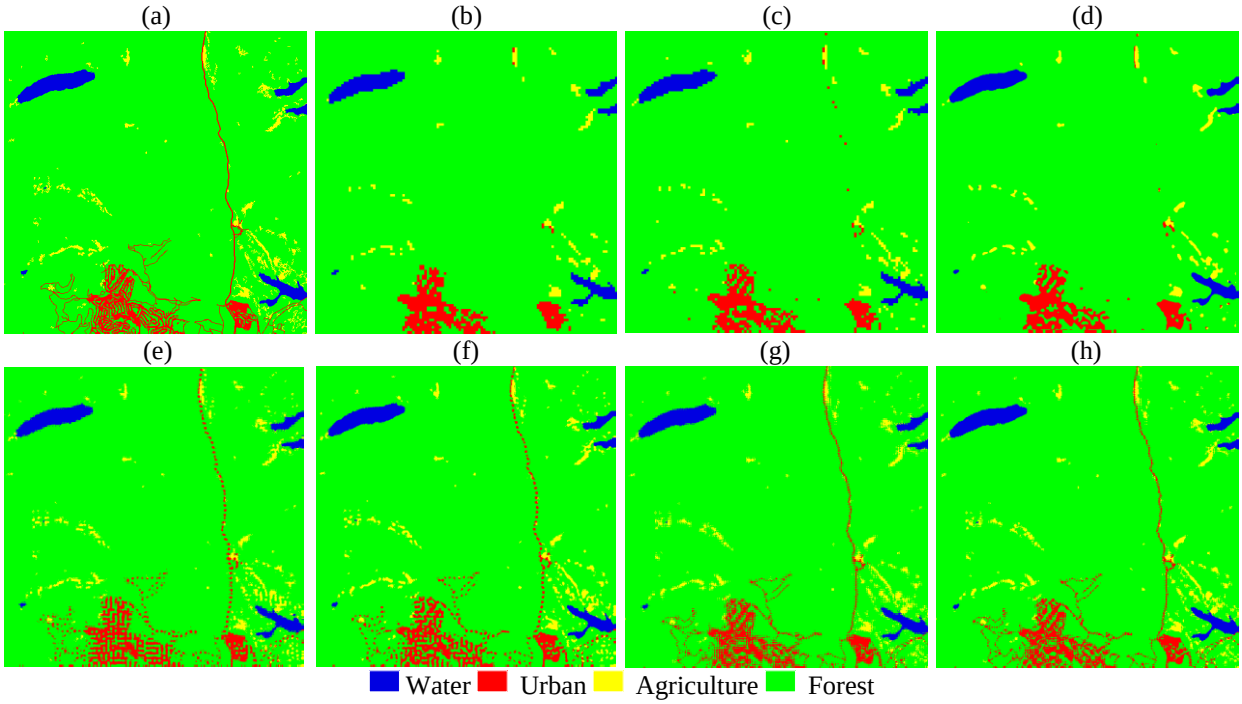

Fig. 7. The SPM results for the California dataset with a zoom factor of 4 (496×496 pixels). (a) Reference. (b) HC-without-PSF. (c) HC-with-PSF. (d) HNN-with-PSF (Gaussian PSF). (e) PSA-without-PSF (i.e., with ideal square PSF). (f) PSA-with-PSF (Gaussian PSF). (g) ATPK-without-PSF (i.e., with ideal square PSF). (h) ATPK-with-PSF (Gaussian PSF).

Overall, after reducing the PSF effect, both PSA and ATPK show more accurate results than the original versions as well as the recently developed HNN-with-PSF method. Moreover, the inter-comparison reveals that by reducing the PSF effect, ATPK can produce visually more accurate predictions (e.g., the linear features of the urban class can be restored more accurately).

3.3. Quantitative evaluation on SPM results using conventional classification-based index

Table 2 lists the OAs of the two HC methods (i.e., HC-without-PSF and HC-with-PSF) and all five SPM methods of both s=4 and s=8 for the three datasets. As observed from the table, for the same method, when the PSF effect is considered, greater accuracy can be produced. For example, all OAs of HC-with-PSF are larger

than those of HC-without-PSF. For the five SPM methods, for the case of s=4 for the Ohio dataset, the OA of ATPK-with-PSF is 0.8951 while the OA of ATPK-without-PSF is 0.8731. The OAs of PSA-with-PSF and PSA-without-PSF are 0.8968 and 0.8672, respectively. The advantage of considering the PSF is also obvious for the other two datasets. For example, by considering the PSF effect, the accuracy gains of both ATPK and PSA are about 0.03 for the South Carolina dataset with s=4. Noticeably, although the OAs of HC results are larger than that those of ATPK-without-PSF and PSA-without-PSF, the visual comparison in Figs. 5-7 reveals that the HC results are substantially different from the reference. Furthermore, contrary to the visual results in Figs. 5-7, where HNN-with-PSF is found to be less accurate, the OAs of HNN-with-PSF are the largest amongst the five methods.

The accuracy for each land cover class was also analyzed, as shown in Figs. 8 and 9, where the PA and UA of the two HC methods and the five SPM methods for the three datasets are provided. Obviously, both the PA and UA of the results produced by considering the PSF are larger than those without considering the PSF; see the difference between the deep blue and yellow bars, the difference between the green and orange bars, and the difference between the blue and magenta bars. For example, with respect to ATPK-with-PSF, the PA values of water, urban, agriculture and forest are increased by about 0.026, 0.031, 0.013 and 0.035, respectively, when compared with ATPK-without-PSF for the Ohio dataset with s=4. As for PSA, the PA values of the four classes are increased by about 0.025, 0.041, 0.014 and 0.040 after considering the PSF. Furthermore, the statistical results for the largest PA or UA in all 24 cases (two zoom factors for each of the three datasets, each of which covers four classes) are provided in Table 3. The results suggest that, in terms of both the PA and UA, HNN-with-PSF produces the greatest accuracy in most cases.

Overall, based on the quantitative analysis in terms of classification accuracy (i.e., PA in Fig. 8, UA in Fig. 9 and OA in Table 1), the HNN-with-PSF method is found to be a more accurate SPM method in most cases. This conclusion, however, conflicts obviously with that drawn from visual inspection in Figs. 5-7 where HNN-with-PSF fails to reproduce many features such as linear features and small-sized patches. Moreover, the boudaries of the HC results in Figs. 5-7 are severely jagged, but the classification accuracies of the HC results

are larger than those for ATPK-without-PSF and PSA-without-PSF in some cases. The conflicts suggest that per-subpixel classification accuracy-based quantitative evaluation cannot fully reflect the quality of the SPM results. Consequently, assessment of SPM in terms of the new error index that integrates both accuracies of classification and spatial structure reproduction is provided below.

Table 2 OAs of the two HC and five SPM methods for the three datasets

	Zoom factor	HC-without-PSF	HC-With-PSF	HNN-with-PSF	PSA-without-PSF	PSA-with-PSF	ATPK-without-PSF	ATPK-with-PSF
Ohio	*s*=4	0.8688	0.8722	**0.9036**	0.8713	0.8974	0.8731	0.8951
	s=8	0.8117	0.8175	**0.8504**	0.7745	0.8180	0.8014	0.8247
South Carolina	*s*=4	0.7896	0.7959	**0.8292**	0.7814	0.8238	0.7902	0.8256
	s=8	0.7091	0.7164	**0.7435**	0.6335	0.6890	0.6824	0.7129
California	*s*=4	0.9532	0.9544	**0.9584**	0.9469	0.9554	0.9513	0.9571
	s=8	0.9422	0.9430	**0.9492**	0.9257	0.9344	0.9325	0.9378

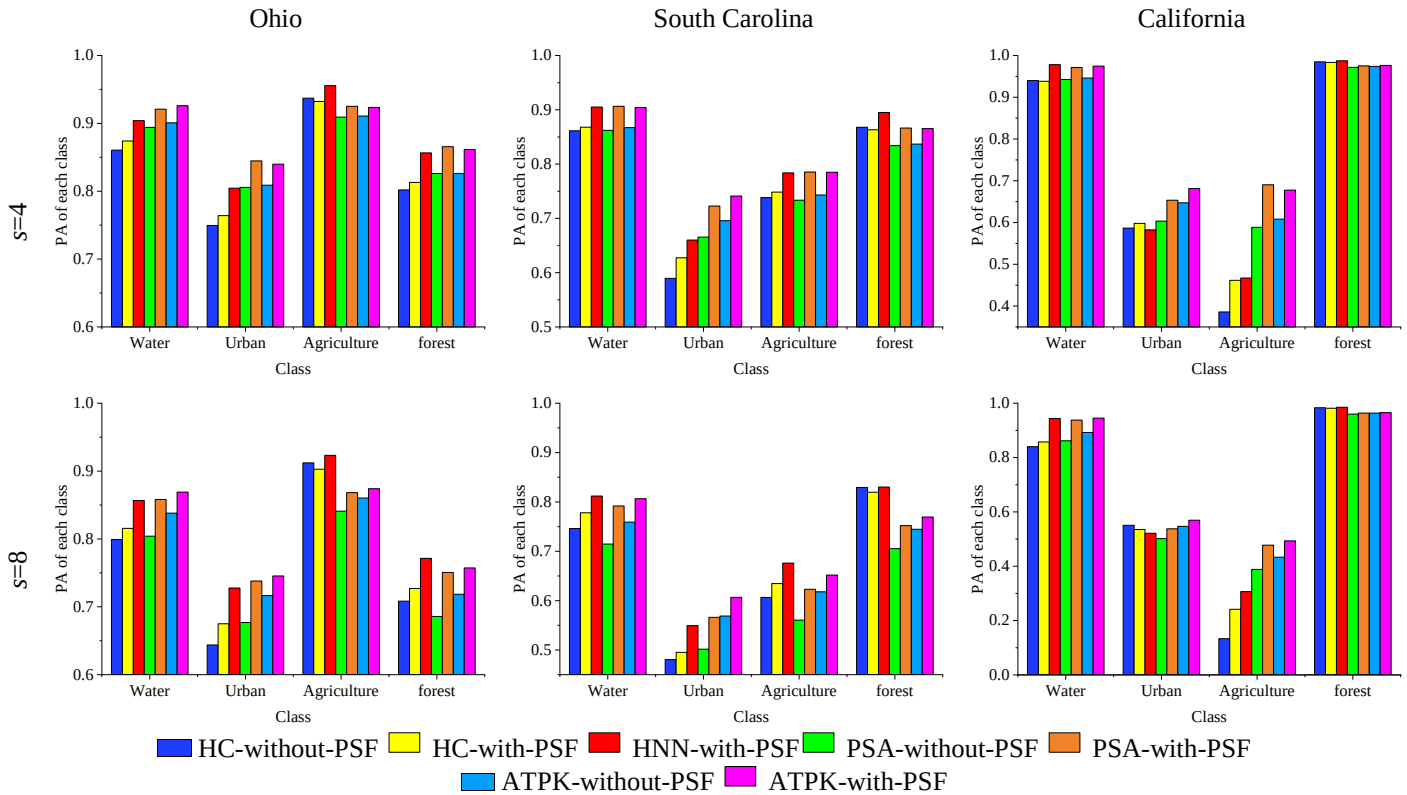

Fig. 8. PA of each class for the three datasets.

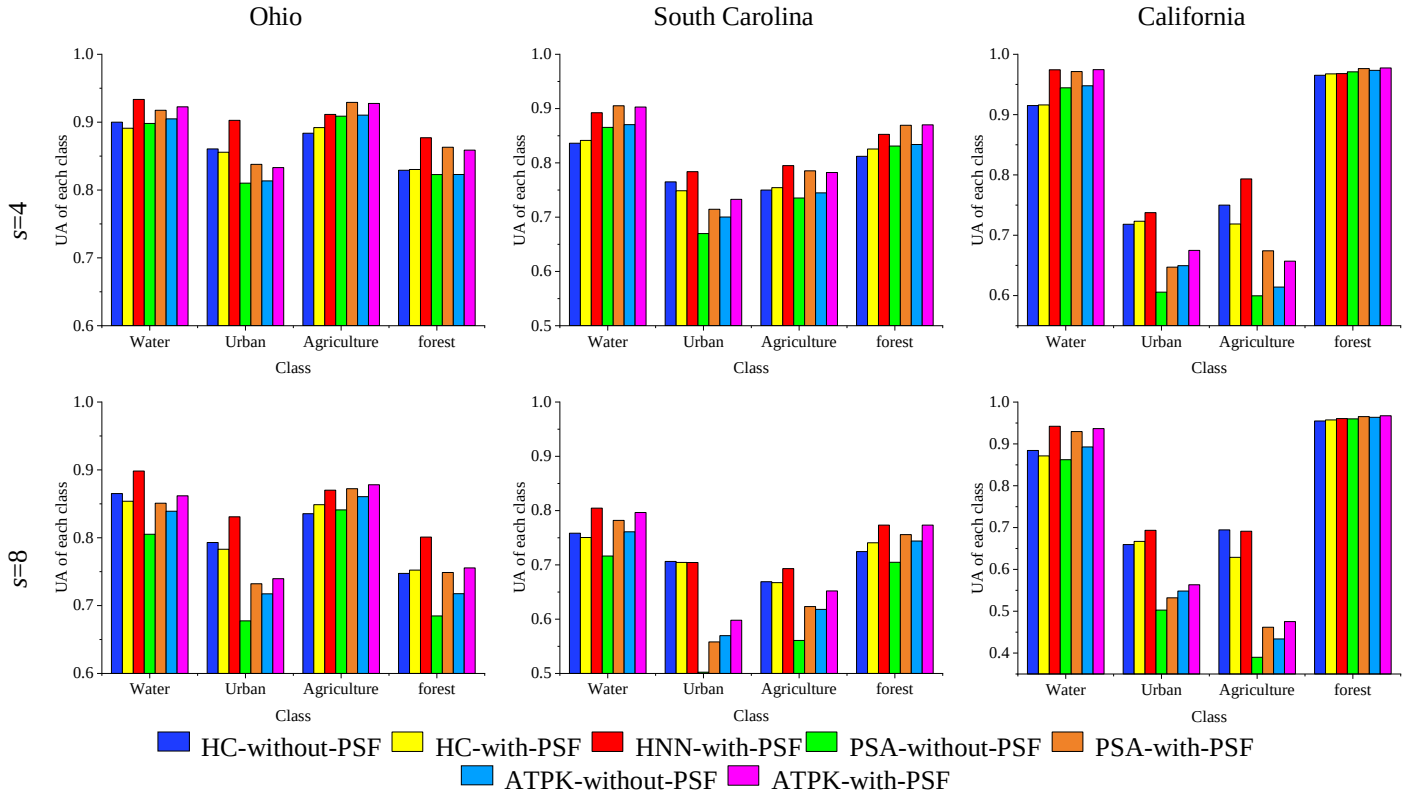

Fig. 9. UA of each class for the three datasets.

Table 3 Statistical results of PA and UA amongst the SPM results

	Cases of largest PA	Cases of largest UA
HNN-with-PSF	10	17
ATPK-with-PSF	9	5
PSA-with-PSF	5	2

3.4. Assessment on SPM in terms of the semivariogram

1) Qualitative evaluation of semivariogram: Fig. 10 shows the semivariograms of the reference maps, the HC results and five SPM results for the three datasets. Through visual checking, the following observations can be made.

First, the semivariograms of the HC methods are very different from those of the SPM methods as well as the references. The reason is that the HC methods produce jagged boudaries and eliminate most of the elongated details. Furthermore, the HNN-with-PSF semivariograms in all cases are the most different from the references, which means that the HNN-with-PSF method is the least accurate amongst all SPM methods in reproducing the reference semivariograms. This is because HNN-with-PSF produces over-smooth results and loses a large

504 number of small-sized patches and linear features, see Figs. 5-7. This leads to obviously smaller spatial
505 variability (i.e., smaller semivariances).

506

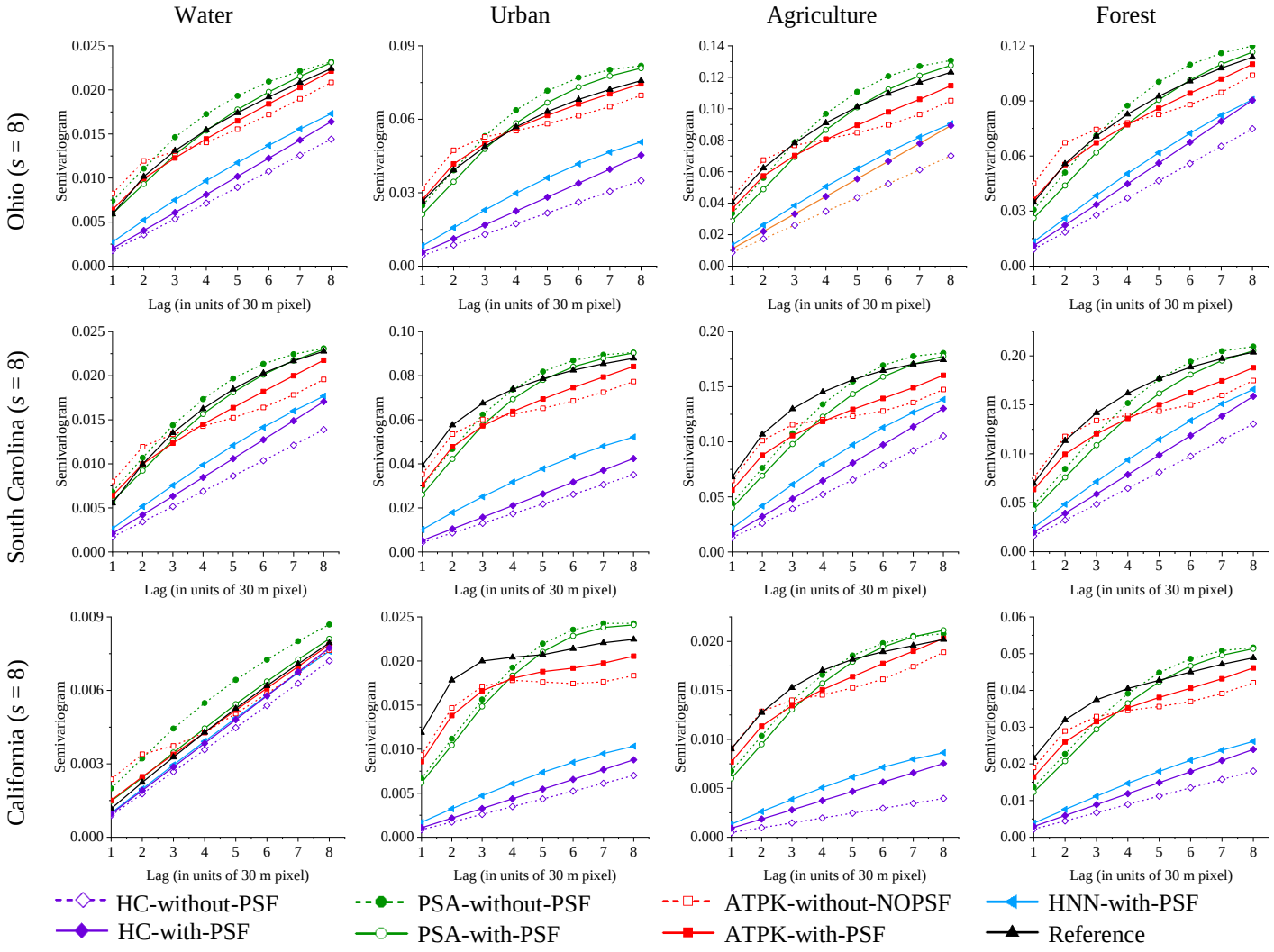

507 Fig. 10. Fine spatial resolution semivariograms of the results of the two HC and five SPM methods for the three datasets.

508

509 Second, compared to the results of ATPK-without-PSF and PSA-without-PSF, the semivariograms of the
510 ATPK-with-PSF and PSA-with-PSF methods are more consistent with those of the references, suggesting that
511 the SPM results are closer to the references and are more accurate. Compared with the visual results in Fig. 5-7,
512 clearer boundaries and more linear features are restored by ATPK-with-PSF and PSA-with-PSF, and the
513 produced spatial structures are more similar to those of the reference maps. Thus, by reducing the PSF effect,
514 both ATPK and PSA can produce more accurate predictions in terms of the semivariogram.

Overall, the abovementioned conclusion based on the semivariogram is consistent with the conclusion drawn from visual inspection in Figs. 5-7. This means that the semivariogram is able to provide a more resonable index for quantitative evaluation of SPM methods in terms of reproducing spatial structure. Hence, the assessment based on the semivariogram is provided below.

2) Quantitative evaluation using the MAE: The MAE of semivariogram is shown in Fig. 11 to evaluate quantitatively the accuracy of semivariograms for each class. It can be concluded from the barcharts that as the PSF effect is considered, the MAE values of both ATPK-with-PSF and PSA-with-PSF decrease. For example, when considering the PSF effect using ATPK for the Ohio dataset with s=4, the MAE values of water, urban, agriculture and forest are reduced by about 0.0005, 0.0006, 0.0017 and 0.0013, respectively.

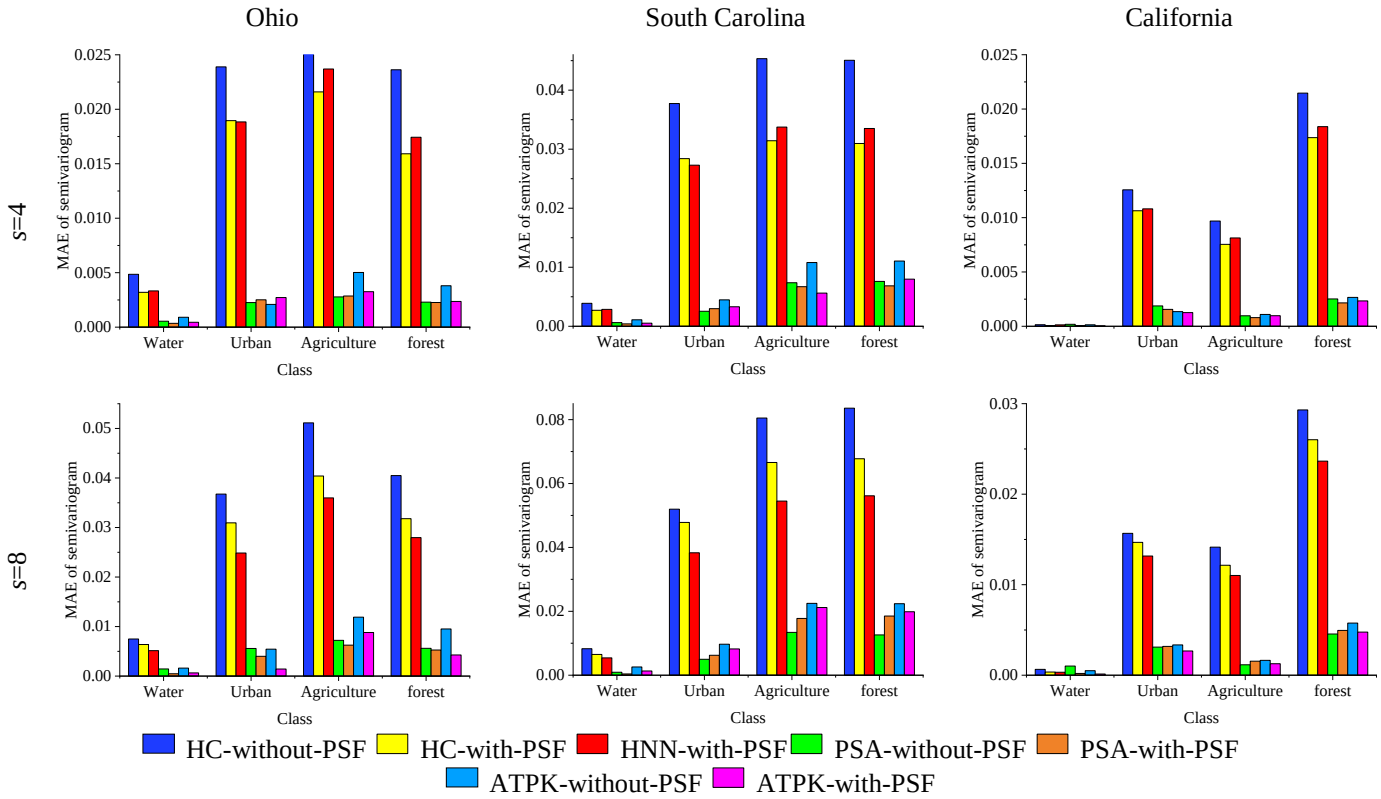

Fig. 11. The MAE of semivariogram of each class for the three datasets.

Furthermore, consistent with the visual assessment of spatial structure in Fig. 10, HNN-with-PSF produces the largest MAE amongst the five SPM methods in most cases because of the loss of small-sized features and over-smooth artifacts. However, for the water class in the California dataset, the MAE of HNN-with-PSF is

smaller than that of PSA-without-PSF and ATPK-without-PSF. The reason for this phenomenon is that the water class is compact in the reference map, which complies with the advantage of HNN in reproducing compact objects. Moreover, the MAEs of the HC results are larger than all SPM results.

In summary, the evaluation based on MAE generally agrees with that of visual comparison of the semivariogram in Fig. 10. Thus, from the perspective of reproducing spatial structure, the MAE of the semivariogram is an appropriate choice for quantitative evaluation.

3.5. Assessment based on the proposed integrated error (IE) index

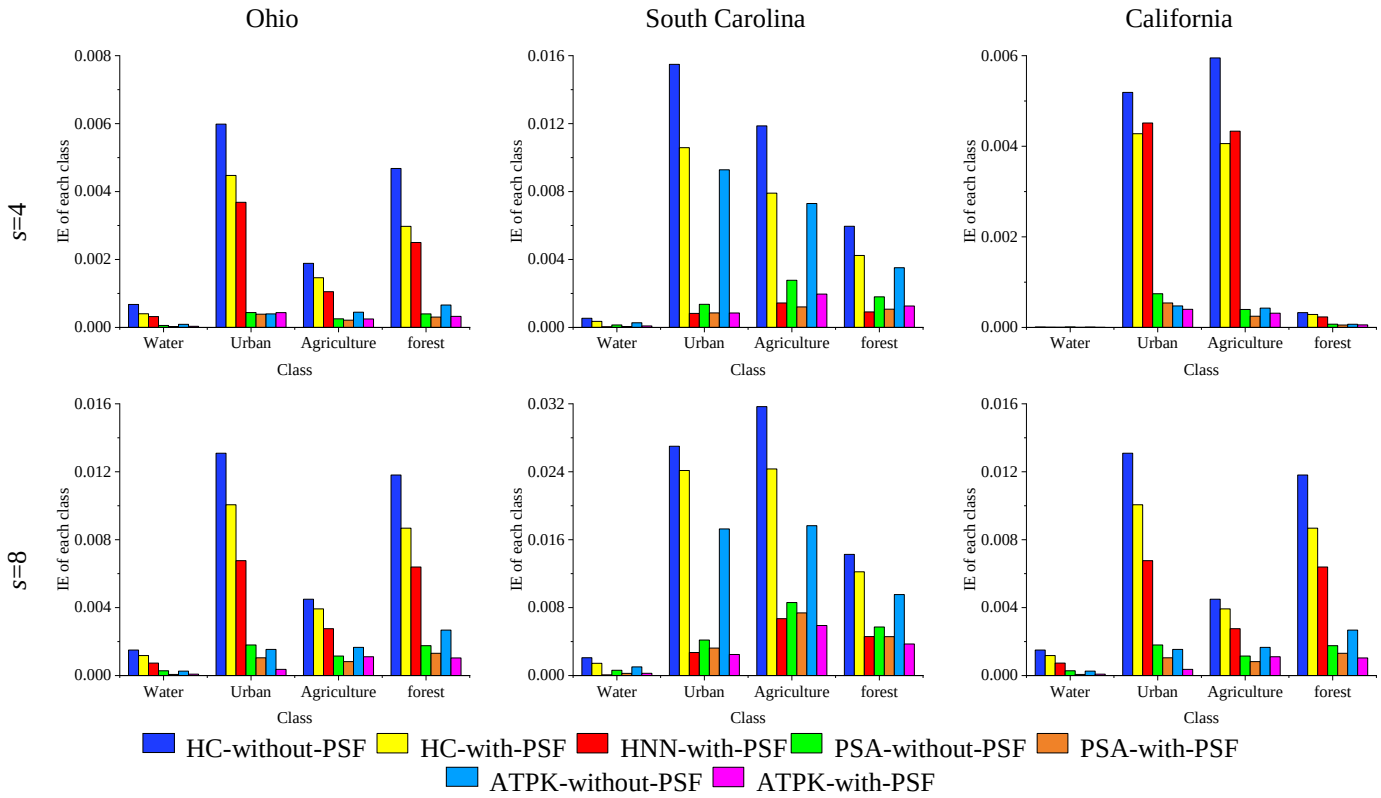

Fig. 12. The proposed IE index of each class for the three datasets.

In this section, the proposed IE index was used to evaluate SPM in terms of both subpixel prediction and spatial structure prediction. As deduced by the visual comparison from the barcharts in Fig. 12, when the PSF effect is considered, much smaller IE values are produced. For example, for the South Carolina dataset with s=4, the IE values of ATPK-with-PSF are 0.0001, 0.0005, 0.0016 and 0.0070 smaller than those of

ATPK-without-PSF for the water, urban, agriculture and forest classes, respectively. Moreover, compared to the HC predictions, the IEs of all SPM predictions are smaller, which means more accurate results are produced by SPM.

In all SPM circumstances, compared to ATPK-with-PSF and PSA-with-PSF, HNN-with-PSF produces the largest IE values, due to the small spatial variation of its over-smooth prediction. This means that the HNN results are less accurate, although they have the largest per-subpixel classification accuracies. Thus, the new index IE-based quantitative evaluation leads to the same conclusion as for visual inspection, suggesting that the new index is a reliable choice for quantitative evaluation of SPM methods.

3.6. Assessment based on computing efficiency

Computational burden is an important factor to evaluate SPM methods. The computing times of the five methods are listed in Table 4. All experiments were performed on an Intel Core i7 with the MATLAB 9.5 version. For PSA, the number of iterations was set to 3000. For HNN-with-PSF, the time step was set to 0.001, the steepness of the *thah* function was set to 10, and the number of iterations was 3500.

Table 4 Consuming time of the five methods (s=8, in units of seconds)

	ATPK-without-PSF	ATPK-with-PSF	HNN-with-PSF	PSA-without-PSF	PSA-with-PSF
Ohio	78	80	60300	36	126
South Carolina	79	81	66400	60	140
California	78	81	24100	51	124

As listed in Table 4, HNN-with-PSF took the longest time (over 10 hours while the other methods took about 1 to 4 minutes). PSA-with-PSF took more time than PSA-without-PSF, as pre-processing is required to predict the enhanced coarse proportions. ATPK (including both ATPK-withour-PSF and ATPK-with-PSF), is generally faster as the subpixel-to-pixel-based method does not require iteration. Therefore, the proposed model can effectively reduce the PSF effect in SPM without scarificing computing efficiency.

3.7. Experiments on the multispectral image

To further examine the effectiveness of the proposed general SPM model and the proposed IE index, a synthesized multispectral image was used in this experiment. Specifically, the 30 m Landsat 7 ETM+ image was used as the original dataset, as shown in Fig. 13(a). The corresponding 30 m reference land cover map was drawn manually, see Fig. 13(b). A multispectral image was synthesized (see Fig. 13(c)) based on the mean and variance of each land cover class in the original 30 m Landsat image in Fig. 13(a). The synthesized multispectral image was upscaled with a factor of 8 using a Guassian PSF to produce a 240 m coarse multispectral image, see Fig. 13(d). More details of the simulation process can be found in Wang and Atkinson (2017). In this way, the uncertainty of the 30 m reference map can be avoided and we can focus solely on the performances of spectral unmixing and SPM.

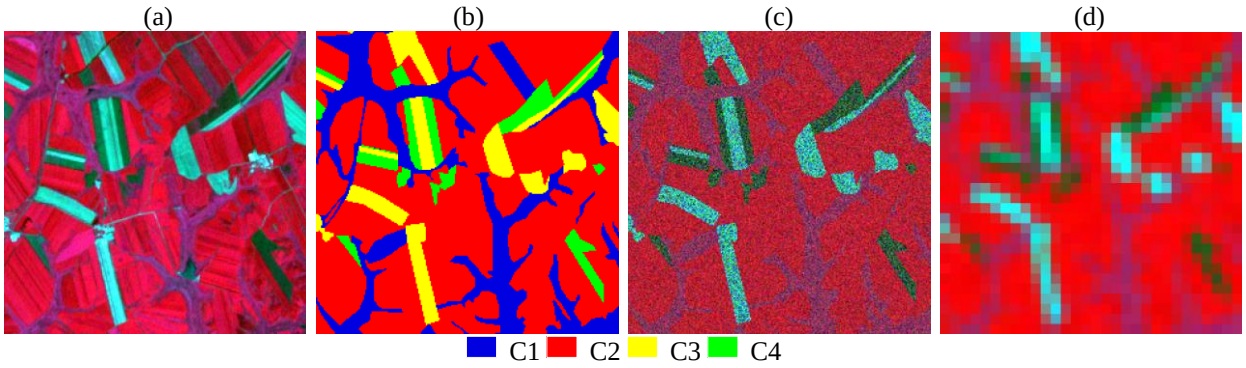

Fig. 13. The multispectral image used in the experiment. (a) Original 30 m Landsat ETM+ image (bands 432 as RGB, 240×240 pixels). (b) 30 m reference land cover map drawn manually from (a) (240×240 pixels). (c) 30 m synthesized multispectral image (bands 432 as RGB, 240×240 pixels). (d) 240 m coarse multispectral image produced by degrading (c) with a Gaussian PSF and a degradation factor of 8 (30×30 pixels).

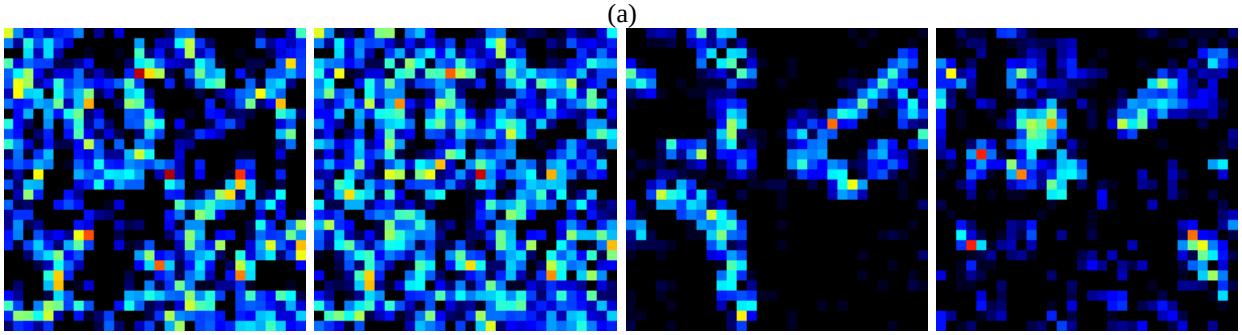

(b)

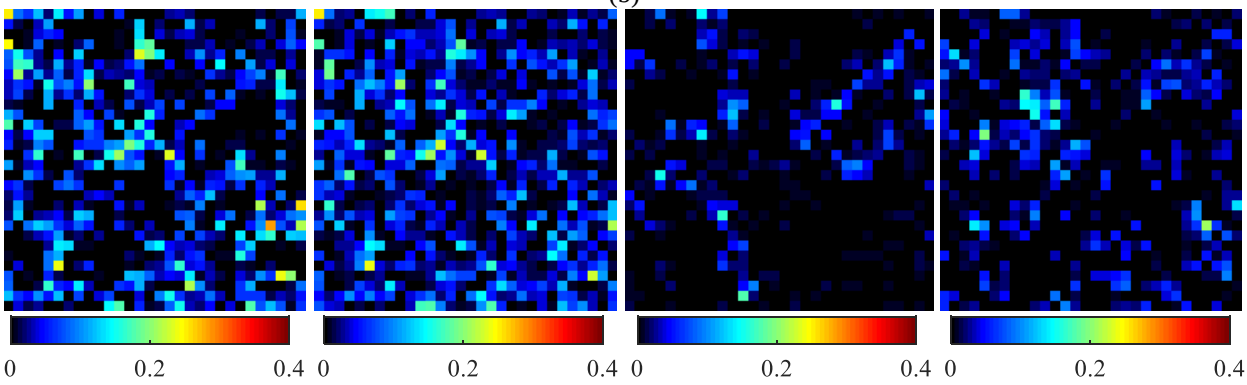

Fig. 14. 240 m proportion error images for the multispectral image (s=8, 30×30 pixels). (a) Absolute value of proportion error between the PSF-contaminated proportion image and the reference. (b) Absolute value of proportion error between the enhanced proportion image and the reference. From left to right are the results for C1, C2, C3 and C4.

The proportion errors (i.e., compared to the reference created by upscaling Fig. 13(b) using a 8×8 square wave filter) of the two types of proportions (i.e., the PSF-contaminated proportion and the enhanced proportion) are shown in Fig. 14(a) and Fig. 14(b). It is seen that the errors are reduced noticeably by considering the PSF effect in spectral unmixing. More precisely, the decreases in RMSEs are about 0.03, 0.04, 0.03 and 0.02 for C1, C2, C3 and C4, respectively. The results of the two HC and five SPM methods are shown in Fig. 15. Three observations can be made from the visual evaluation. First, all five SPM methods produce more elegant boundaries than HC, suggesting the advantages of SPM. Second, failing to account for the PSF effect, ATPK-without-PSF and PSA-without-PSF predictions are occupied by spurs on the boundaries of the land cover objects. By considering the PSF effect, the ATPK-with-PSF and PSA-with-PSF predictions are closer to the reference. For example, the boundaries in Fig. 15(e) are jagged and many noisy patches exist, but those for PSA-with-PSF in Fig. 15(f) are more continous, especially for classes C2 and C3. As the HNN-with-PSF method is not completely slavish to the coarse proportions, it can remove noisy artifacts and produce a smooth result. However, as marked by the white circle, the linear features (e.g., for class C1) are incorrectly predicted as crowed patches by the HNN-with-PSF and some of them even disappear; see Fig. 15(d). In contrast, these linear features are reproduced satisfactorily by PSA-with-PSF and ATPK-with-PSF, see Fig. 15(f) and Fig. 15(h).

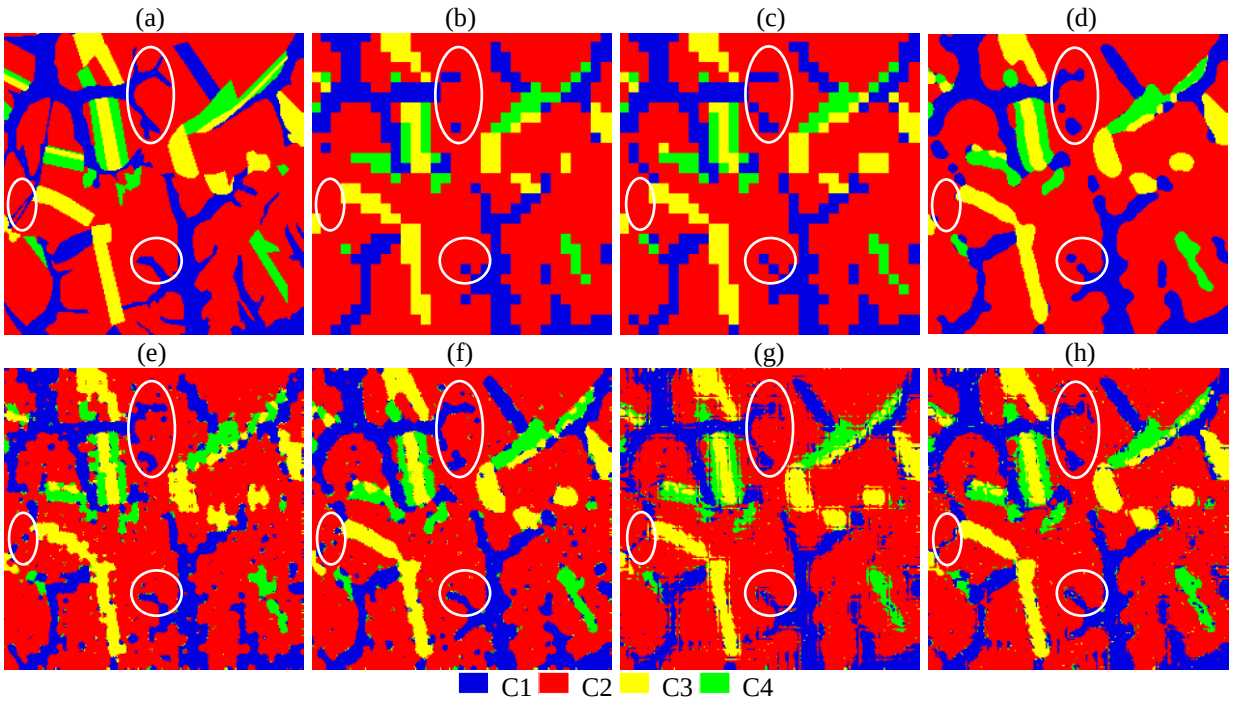

Fig. 15. The SPM results for the multispectral image with a zoom factor of 8 (240×240 pixels). (a) Reference. (b) HC-without-PSF. (c) HC-with-PSF. (d) HNN-with-PSF (Gaussian PSF). (e) PSA-without-PSF (i.e., with ideal square PSF). (f) PSA-with-PSF (Gaussian PSF). (g) ATPK-without-PSF (i.e., with ideal square PSF). (h) ATPK-with-PSF (Gaussian PSF).

The OAs of the methods are listed in Table 5. The OAs of PSA-with-PSF and ATPK-with-PSF are 0.8916 and 0.8905, with a gain of about 0.03 over those produced without considering the PSF effect. However, contrary to the visual evaluation where HNN-with-PSF is found to be over-smooth and less accurate, the OA of HNN-with-PSF is the largest among the five SPM methods. The semivariograms of all results are shown in Fig. 16. It can be observed that the ATPK-with-PSF and PSA-with-PSF semivariograms are closer to the reference than both HC and HNN-with-PSF, indicating that more accurate spatial structure is reproduced. Furthermore, based on the proposed IE index, as provided in Fig. 17, ATPK-with-PSF and PSA-with-PSF tend to be more accurate. The conclusion is consistent with that drawn from visual comparison. Therefore, the proposed general solution to reduce the PSF effect in SPM is also applicable to the more challenging case (i.e., SPM of original multispectral images) and, further, the IE index is a feasible comprehensive choice for quantitative evaluation of SPM methods.

Table 5 OAs of the five SPM methods for the multispectral image

	HC-without-PSF	HC-with-PSF	HNN-with-PSF	PSA-without-PSF	PSA-with-PSF	ATPK-without-PSF	ATPK-with-PSF
OA	0.8495	0.8542	**0.9186**	0.8595	0.8916	0.8634	0.8905

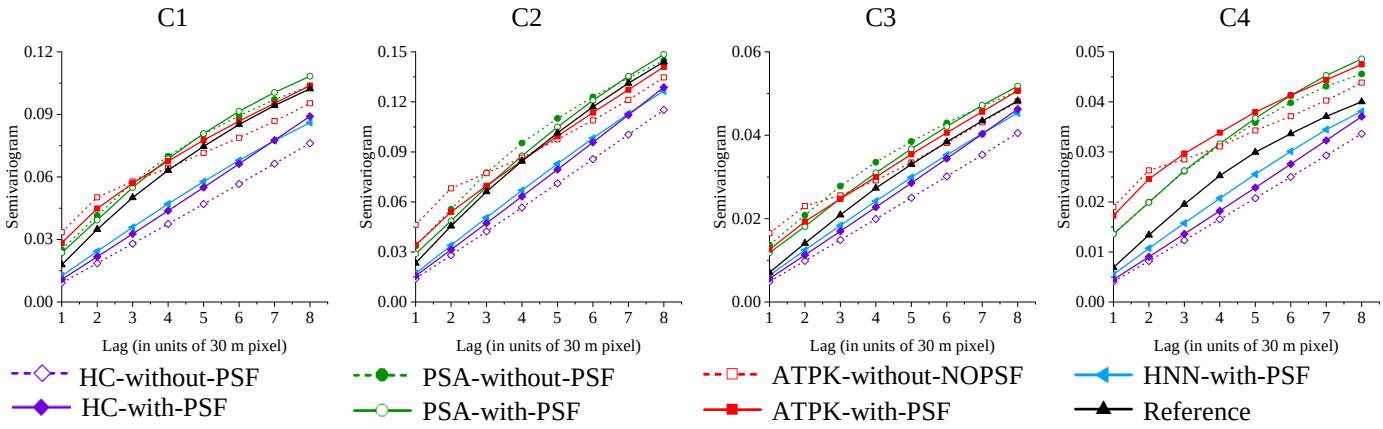

Fig. 16. Fine spatial resolution semivariograms of the results of the two HC and five SPM methods for the multispectral image.

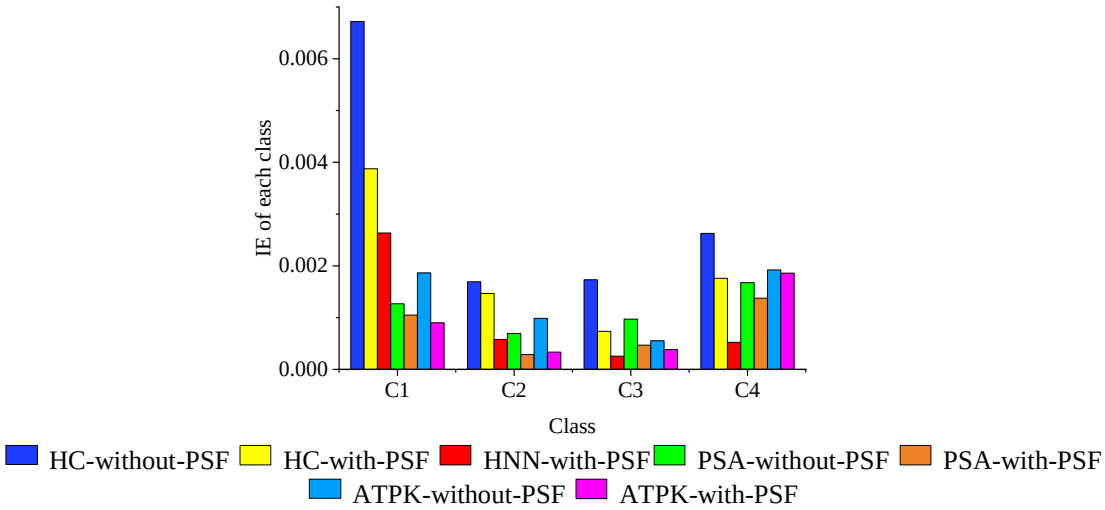

Fig. 17. The proposed IE index of each class for the multispectral image.

4. Discussion

4.1. Generalization ability of the proposed SPM model

The proposed general model that considers the PSF effect is not designed for a specific SPM method, but any method where spectral unmixing predictions can be slotted in. To investigate the model performance in the

experiments, two typical SPM methods (i.e., PSA and ATPK) were considered and the performances were compared with the HNN-with-PSF method developed in our previous research (Wang and Atkinson, 2017). Theoretically, the ATPK-with-PSF method should use ATPK twice, first to produce the enhanced coarse proportions by considering the PSF effect, and second to downscale the coarse proportions in SPM. However, the differences between the two ATPK results for the three datasets used in the experiments were found to be very small (i.e., the differences in CCs are smaller than 0.0020). Thus, ATPK was used only once in the experiments in this paper. The experimental results show that the enhanced coarse proportion is an important premise of SPM. Exploiting this capability, the proposed model is applicable for many existing methods, including subpixel-to-pixel-based (e.g., RBF (Wang et al., 2014a) and SPSAM (Mertens et al., 2006)), subpixel-to-subpixel-based methods (e.g., GA (Mertens et al., 2003) and MAP (Zhong et al., 2015)) and also hybrid methods combining these two types of dependencies (Chen et al., 2018a; Ling et al., 2014). Based on this character and encouraging performances of the ATPK- and PSA-based methods in this paper, in future research, it would be interesting to conduct a systematic study by comparing all existing SPM methods to identify the most effective solutions to reduce the PSF effect. Moreover, it is undoubtedly worthwhile to examine the performance in tackling the PSF effect when developing more advanced SPM methods in future.

4.2. Solutions to one stage SPM

This paper demonstrated the use of enhanced coarse proportions to be an effective strategy for SPM, which is essentially a two-stage approach composed of enhancing spectral unmixing by reducing the influence of the PSF effect and SPM based on the enhanced coarse proportions. The uncertainty in the first stage can be propagated to the second stage directly. To control the uncertainty in both spectral unmixing and SPM jointly, it would be worthwhile to develop a one-stage SPM model that can account for the PSF directly in SPM. The spatial-spectral model, such as Markov random field (MRF)-based method (Tolpekin and Stein, 2009), facilitates to SPM from original multispectral images in one stage through considering spatial dependences and spectral constraints simultaneously. When adopting the one stage spatial-spectral SPM model for reducing the

influence of the PSF effect, the PSF can be considered in the spectral term, where the PSF-convolved spectra of interim SPM realizations need to be compared to the original coarse spectra and the difference used to guide optimization. However, there may be several challenges. First, no theory is universally applicable for estimating the parameter controlling the spatial and spectral parts, which remains an open problem. The over-parameterized spatial-spectral model may lead to tendentious fitting, resulting in lower accuracy for SPM. Specifically, over-weighting the spatial term may lead to an over-smooth result, which is disadvantageous for preserving spatial detail. Conversely, over-weighting the spectral term may fail to account for spatial correlation, resulting in discontinuous artifacts with noise. Second, similar to HNN, the spatial term of the MRF is always defined based on local smoothness, which means the MRF is more suitable for homogeneous areas. For areas with strong heterogeneity and dominated by small patches and elongated features, a more appropriate spatial term needs to be defined. This may require additional data or prior information. Finally, when considering the PSF effect by the one stage spatial-spectral model, subpixels in the neighboring coarse pixels are also involved in characterizing the spectral term. Convergence of the spatial-spectral model may not be achieved when more subpixels are involved in optimization.

4.3. Uncertainties in HNN

In this paper, the HNN-with-PSF method from previous research was used as a benchmark for comparison in the experiments. It should be noted, however, that the HNN was not originally designed for linear features and small-sized patches, and the spatial correlation is characterized based on an eight-neighborhood which is suitable for the H-resolution case (i.e., most of the coarse pixels are smaller than the objects of interest). For the L-resolution case (i.e., the objects of interest fall within a coarse pixel) (Atkinson, 2009), the alternative pattern matching-based HNN (Tatem et al., 2002) is a more appropriate choice to reproduce small-sized features. However, a training dataset or auxiliary information at the target fine spatial resolution is required for this type of HNN. Additionally, the spatial pattern in the prior knowledge needs to be sufficiently similar to that of the target area. This is not the case for PSA and ATPK as used in this paper, which can be performed without any

additional dataset. Thus, for fair comparison, the H-resolution HNN model was applied in this paper, as was done in (Wang and Atkinson, 2017). Certainly, although such additional data for the L-resolution HNN are difficult to acquire in general, their value for enhancement should be borne in mind.

4.4. Uncertainties in accuracy assessment

1) Uncertainties in the semivariogram function: Although the semivariogram was shown to be effective for evaluating the reproduction of spatial structure, there are still uncertainties that should be noted. First, in the experiments, the semivariogram for quantitative evaluation is assumed to be a scalar which only evaluates the difference in categorical values between a pixel and its neighbors in four directions. As acknowledged widely, land cover features are sometimes direction-dependent. Therefore, calculating the semivariogram separately for different directions seems to be a more reasonable choice. However, it is unclear how greatly the consideration of directions will increase the reliability of reflecting spatial structure, as the assumption of a scalar has been commonly used in geostatistics. Second, although curve-fitting is generally adopted for semivariograms (especially in kriging interpolation), uncertainty exists in the fitting process (e.g., different choices for fitting functions). The reliability of the semivariogram is crucial for small lags, which plays key role in reflecting spatial structure. If curve-fitting is required, it would be more appropriate to consider a weighting scheme that gives larger weights for semivariograms at small lags, rather than the conventional equal scheme. It would be important to determine the weights reliably. In addition, it should be noted that for ATPK, the input of the fine-to-fine semivariogram is estimated by deconvolution of the coarse semivariogram extracted from the coarse proportion image, as performed in this paper. For accuracy assessment based on the semivariogram, the reference semivariogram is normally calculated using the reference land cover map. When such a reference map is unavailable (i.e., an unsupervised case), the estimated fine-to-fine semivariogram might be used for accuracy assessment. In this case, the accuracy will also be a function of the deconvolution.

2) Alternatives to the semivariogram: The semivariogram captures only the differences between two points (e.g., A to B and B to A lead to the same difference) (Atkinson, 2009). Alternatively, the two-point histogram

(Atkinson, 2004) can distinguish directional differences and captures strictly double the information of the semivariogram. However, two-point statistics are weak in characterizing continuous spatial patterns (e.g., river and roads). Multi-point statistics (MPS) (Mariethoz et al., ,2010) characterize the relations between multiple points simultaneously based on a template and, thus, captures more information than traditional two-point statistics. Thus, it would be worthwhile to consider MPS for accuracy evaluation of SPM in future research.

3) Considerations of the proposed integrated error index: The results presented in this paper validate the reliability of the proposed integrated error index. Two issues can be borne in mind for further possible refinements. First, in the integrated error index, we used an accuracy index PA for evaluating the performance of subpixel level classification, rather than UA of each class. This is because the denominator in calculating UA is the total number of pixels for each class in the resulting map, while the denominator for PA is that in the reference map. Thus, when calculating the classification accuracy using PA, only the numerator (i.e., the number of correctly classified pixels) varies and the denominator is fixed for each method. This is different from UA, in which both the numerator and denominator vary. This can lead to an unreasonably large accuracy in some cases. For example, the UA of the target in Fig. 2(c) is 100%, which means it is perfectly correctly classified. From visual inspection, however, this accuracy is inappropriate. Therefore, compared to PA, the uncertainty in using UA for the integrated index is larger and PA is more appropriate for further integrated accuracy assessment.

Second, the idea of the new index can be generalized as $f_k(MAE_k, 1-PA_k)$ where $f_k(\bullet)$ presents the accuracy for land cover class *k*, MAE_k of semivariogram evaluates the reproduction of spatial pattern and $1-PA_k$ evaluates the classification error for class *k*. This releases the space for defining more advanced indices and opens new avenues for SPM evaluation. For example, other functions can be developed as alternatives to the multiplication operator in this paper. It would also be interesting to explore effective solutions to determine the weighting parameters more reasonably. In addition, indices such as the structure similarity index measure (SSIM) (Wang et al., 2004) and intersection over union (IoU) (Rezatofighi et al., 2019) that can evaluate the similarity between spatial structures can also be potentially considered in future research.

752

753 *4.5. Utilization of auxiliary data*

754 The proposed model enhances SPM by considering the PSF effect, where no auxiliary information is
755 required. As an ill-posed problem, however, uncertainty exists inevitably in SPM and effective usage of
756 supplementary information has generally been a focus of SPM. Various sources of additional information have
757 been used to tackle the uncertainty issue in SPM over the past decades, such as digital elevation models (DEM)
758 (Ling et al., 2008), multiple shifted images (Ling et al., 2010; Wang et al., 2017), point constraints (Wang et al.,
759 2020), height information from Light Detection And Ranging (LiDAR) elevation (Nguyen et al., 2005),
760 training images (Jia et al., 2019; Ling and Foody, 2019), and panchromatic images (Nguyen et al., 2011).
761 Recently, temporal information from time-series images shows great potential in SPM as well (Li et al., 2017;
762 Zhang et al., 2017). All these data have great potential in enhancing the proposed general SPM model where
763 the supplementary information has not been incorporated yet. How to control jointly the influences of the
764 auxiliary data and the PSF is a critical issue.

765

766 **5. Conclusion**

767

768 The PSF effect, which is ubiquitous in optical remote sensing, influences SPM greatly and has been a main
769 obstacle to increase the accuracy of subpixel land cover maps. However, it has seldom been considered in
770 existing SPM methods. The recently developed HNN-with-PSF method (Wang and Atkinson, 2017) is one of
771 the very few examples tackling the PSF issue in SPM. However, the method fails to restore small-sized patches
772 and produces over-smooth predictions. Moreover, it is computationally expensive. This paper proposed a
773 general model to reduce the influence of the PSF effect in SPM. The proposed model considers the PSF effect
774 in the pre-spectral unmixing process, and is suitable for any SPM method which uses spectral unmixing
775 predictions as input.

SPM is a technique for both classification and downscaling. In the existing SPM literature, however, accuracy assessment is performed based solely on classification, ignoring the ability to reproduce spatial structure in the downscaling process. The classification accuracies of some SPM predictions can be very large, but may fail to reproduce spatial structure satisfactorily (e.g., some small-sized patches and linear features are lost entirely, or the shape of the predicted objects is substantially different from the reference). To fill this need, a new index considering both aspects was proposed for more reliable quantitative evaluation of SPM.

Experiments on four datasets were performed for validation of the proposed SPM model and error index. Five methods (i.e., HNN-with-PSF, PSA-without-PSF, PSA-with-PSF, ATPK-without-PSF and ATPK-with-PSF) were examined. The conclusions are as follows.

1) The proposed SPM model is an effective solution for reducing the PSF effect. From both qualitative and quantitative assessment, the proposed model can produce more accurate SPM predictions than those without considering the PSF effect.
2) The proposed general model accounting for the PSF effect is applicable for both subpixel-to-pixel-based (e.g., ATPK in this paper) and subpixel-to-subpixel-based (e.g., PSA in this paper) methods. Both extended versions outperform the recently developed HNN-with-PSF method by reproducing more small-sized patches and more accurate spatial structure.
3) The discrepancy between visual evaluation and conventional classification-based accuracy reveals that the classification-based index fails to evaluate the reproduction of spatial structure in SPM. The proposed integrated error index combining both subpixel prediction accuracy and spatial structure prediction accuracy is more appropriate, and is more consistent with the conclusion from visual inspection.
4) The proposed model is computationally much faster than the recently developed HNN-with-PSF method.

Acknowledgment

This work was supported by National Natural Science Foundation of China under Grant 41971297,

Fundamental Research Funds for the Central Universities under Grant 02502150021 and Tongji University under Grant 02502350047. The authors would like to thank the anonymous reviewers for their valuable and constructive comments which greatly improved this manuscript.

References

Atkinson, P.M. (1997). Mapping subpixel boundaries from remotely sensed images. Innovations in Gis, 4, 166-180.

Atkinson, P.M. (2004). Super-resolution land cover classification using the two-point histogram. GeoENV IV-Geostatistics for Environmental Applications, 15-28.

Atkinson, P.M. (2005). Sub-pixel target mapping from soft-classified, remotely sensed imagery. Photogrammetric Engineering & Remote Sensing, 71, 839-846.

Atkinson, P.M. (2009). Issues of uncertainty in super-resolution mapping and their implications for the design of an inter-comparison study. International Journal of Remote Sensing, 30, 5293-5308.

Balaguer-Beser, A., Ruiz, L.A., Hermosilla, T., & Recio, J.A. (2013). Using semivariogram indices to analyse heterogeneity in spatial patterns in remotely sensed images. Computers & Geosciences, 50, 115-127.

Chen, Y., Ge, Y., Chen, Y., Jin, Y., & An, R. (2018a). Subpixel land cover mapping using multiscale spatial dependence. IEEE Transactions on Geoscience and Remote Sensing, 56, 5097-5106.

Chen, Y., Ge, Y., Heuvelink, G.B.M., An, R., & Chen, Y. (2018b). Object-based superresolution land-cover mapping from remotely sensed imagery. IEEE Transactions on Geoscience and Remote Sensing, 56, 328-340.

Chen, Y., Xu, L., Fang, Y., Peng, J., Yang, W., Wong, A., & Clausi, D.A. (2020). Unsupervised bayesian subpixel mapping of hyperspectral imagery based on band-weighted discrete spectral mixture model and markov random field. IEEE Geoscience and Remote Sensing Letters, 1-5.

Curran, P. (1988). The semi-variogram in remote sensing: An introduction. Remote Sensing of Environment, 24, 493-507.

Fisher, P. (1997). The pixel: A snare and a delusion. International Journal of Remote Sensing, 18, 679-685.

Foody, G.M. (2002). Status of land cover classification accuracy assessment. Remote Sensing of Environment, 80, 185-201.

Ge, Y., Jin, Y., Stein, A., Chen, Y., Wang, J., Wang, J., Cheng, Q., Bai, H., Liu, M., & Atkinson, P. (2019). Principles and methods of scaling geospatial earth science data. Earth-Science Reviews, 197, 102897.

Rezatofighi, H., Tsoi, N., Gwak, J., Sadeghian, A., Reid, I., & Savarese, S. (2019). Generalized intersection over union: A metric and a loss for bounding box regression. In *CVPR*, 658-666.

Huang, C., Townshend, J.R.G., Liang, S., Kalluri, S.N.V., & DeFries, R.S. (2002). Impact of sensor's point spread function on land cover characterization: Assessment and deconvolution. Remote Sensing of Environment, 80, 203-212.

Jia, Y., Ge, Y., Chen, Y., Li, S., Heuvelink, B.M.G., & Ling, F. (2019). Super-resolution land cover mapping based on the convolutional neural network. Remote Sensing, 11, 1815.

Jin, H., Mountrakis, G., & Li, P. (2012). A super-resolution mapping method using local indicator variograms. International Journal of Remote Sensing, 33, 7747-7773.

Kaiser, G., & Schneider, W. (2008). Estimation of sensor point spread function by spatial subpixel analysis. International Journal of Remote Sensing, 29, 2137-2155.

Kyriakidis, P.C. (2004). A geostatistical framework for area-to-point spatial interpolation. Geographical Analysis, 36, 259-289.

Li, X., Ling, F., Du, Y., & Zhang, Y. (2014). Spatially adaptive superresolution land cover mapping with multispectral and panchromatic images. IEEE Transactions on Geoscience and Remote Sensing, 52, 2810-2823.

Li, X., Ling, F., Foody, G.M., Ge, Y., Zhang, Y., & Du, Y. (2017). Generating a series of fine spatial and temporal resolution land cover maps by fusing coarse spatial resolution remotely sensed images and fine spatial resolution land cover maps. Remote Sensing of Environment, 196, 293-311.

Ling, F., Du, Y., Li, X., Zhang, Y., Xiao, F., Fang, S., & Li, W. (2014). Superresolution land cover mapping with multiscale information by fusing local smoothness prior and downscaled coarse fractions. IEEE Transactions on Geoscience and Remote Sensing, 52, 5677-5692.

Ling, F., Du, Y., Xiao, F., Xue, H., & Wu, S. (2010). Super-resolution land-cover mapping using multiple sub-pixel shifted remotely sensed images. International Journal of Remote Sensing, 31, 5023-5040.

Ling, F., & Foody, G.M. (2019). Super-resolution land cover mapping by deep learning. Remote Sensing Letters, 10, 598-606.

Ling, F., Li, X., Xiao, F., Fang, S., & Du, Y. (2012). Object-based sub-pixel mapping of buildings incorporating the prior shape information from remotely sensed imagery. International Journal of Applied Earth Observation and Geoinformation, 18, 283-292.

Ling, F., Xiao, F., Du, Y., Xue, H.P., & Ren, X.Y. (2008). Waterline mapping at the subpixel scale from remote sensing imagery with high‐resolution digital elevation models. International Journal of Remote Sensing, 29, 1809-1815.

Ma, X., Hong, Y., Song, Y., & Chen, Y. (2019). A super-resolution convolutional-neural-network-based approach for subpixel mapping of hyperspectral images. IEEE Journal of Selected Topics in Applied Earth Observations and Remote Sensing, 12, 4930-4939.

858 Mariethoz, G., Renard, P., & Straubhaar, J. (,2010). The direct sampling method to perform multiple-point geostatistical simulations.
859 Water Resources Research, 46, W11530.
860 Markham, B. (1985). The landsat sensors' spatial responses. IEEE Transactions on Geoscience and Remote Sensing, GE-23,
861 864-875.
862 Mertens, K.C., de Baets, B., Verbeke, L.P.C., & de Wulf, R.R. (2006). A sub-pixel mapping algorithm based on sub‐pixel/pixel
863 spatial attraction models. International Journal of Remote Sensing, 27, 3293-3310.
864 Mertens, K.C., Verbeke, L.P.C., Ducheyne, E.I., & De Wulf, R.R. (2003). Using genetic algorithms in sub-pixel mapping.
865 International Journal of Remote Sensing, 24, 4241-4247.
866 Nguyen, Q.M., Atkinson, P.M., & Lewis, H.G. (2005). Superresolution mapping using a hopfield neural network with lidar data.
867 IEEE Geoscience and Remote Sensing Letters, 2, 366-370.
868 Nguyen, Q.M., Atkinson, P.M., & Lewis, H.G. (2011). Super-resolution mapping using hopfield neural network with panchromatic
869 imagery. International Journal of Remote Sensing, 32, 6149-6176.
870 Peng, J., Liu, Q., Wang, L., Liu, Q., Fan, W., Lu, M., & Wen, J. (2015). Characterizing the pixel footprint of satellite albedo products
871 derived from modis reflectance in the heihe river basin, china. Remote Sensing, 7, 6886-6907.
872 Settle, J.J. (2005). On the residual term in the linear mixture model and its dependence on the point spread function. IEEE
873 Transactions on Geoscience and Remote Sensing, 43, 398-401.
874 Tatem, A.J., Lewis, H.G., Atkinson, P.M., & Nixon, M.S. (2001). Super-resolution target identification from remotely sensed images
875 using a hopfield neural network. IEEE Transactions on Geoscience and Remote Sensing, 39, 781-796.
876 Tatem, A.J., Lewis, H.G., Atkinson, P.M., & Nixon, M.S. (2002). Super-resolution land cover pattern prediction using a hopfield
877 neural network. Remote Sensing of Environment, 79, 1-14.
878 Tolpekin, V.A., & Stein, A. (2009). Quantification of the effects of land-cover-class spectral separability on the accuracy of
879 markov-random-field-based superresolution mapping. IEEE Transactions on Geoscience and Remote Sensing, 47, 3283-3297.
880 Townshend, J.R.G., Huang, C., Kalluri, S.N.V., Defries, R.S., Liang, S., & Yang, K. (2000). Beware of per-pixel characterization of
881 land cover. International Journal of Remote Sensing, 21, 839-843.
882 Van der Meer, F. (2012). Remote-sensing image analysis and geostatistics. International Journal of Remote Sensing, 33, 5644-5676.
883 Verhoeye, J., & De Wulf, R. (2002). Land cover mapping at sub-pixel scales using linear optimization techniques. Remote Sensing of
884 Environment, 79, 96-104.
885 Wang, P., Wang, L., Mura, M.D., & Chanussot, J. (2017). Using multiple subpixel shifted images with spatial–spectral information
886 in soft-then-hard subpixel mapping. IEEE Journal of Selected Topics in Applied Earth Observations and Remote Sensing, 10,
887 2950-2959.

888 Wang, Q., & Atkinson, P.M. (2017). The effect of the point spread function on sub-pixel mapping. Remote Sensing of Environment,
889 193, 127-137.
890 Wang, Q., Shi, W., & Atkinson, P.M. (2014a). Sub-pixel mapping of remote sensing images based on radial basis function
891 interpolation. ISPRS Journal of Photogrammetry and Remote Sensing, 92, 1-15.
892 Wang, Q., Shi, W., & Atkinson, P.M. (2018). Enhancing spectral unmixing by considering the point spread function effect. Spatial
893 Statistics, 28, 271-283.
894 Wang, Q., Shi, W., & Wang, L. (2014b). Allocating classes for soft-then-hard subpixel mapping algorithms in units of class. IEEE
895 Transactions on Geoscience and Remote Sensing, 52, 2940-2959.
896 Wang, Q., Zhang, C., & Atkinson, P.M. (2020). Sub-pixel mapping with point constraints. Remote Sensing of Enviroment, 244,
897 111817.
898 Wang, Z., Bovik, A.C., Sheikh, H.R., & Simoncelli, E.P. (2004). Image quality assessment: From error visibility to structural
899 similarity. IEEE Transactions on Image Processing, 13, 600-612.
900 Wu, K., Niu, R., Wang, Y., Zhang, L., & Du, B. (2011). Super-resolution land-cover mapping based on the selective endmember
901 spectral mixture model in hyperspectral imagery. Optical Engineering, 50, 126201.
902 Wu, S., Ren, J., Chen, Z., Jin, W., Liu, X., Li, H., Pan, H., & Guo, W. (2018). Influence of reconstruction scale, spatial resolution and
903 pixel spatial relationships on the sub-pixel mapping accuracy of a double-calculated spatial attraction model. Remote Sensing of
904 Environment, 210, 345-361.
905 Xu, X., Tong, X., Plaza, A., Li, J., Zhong, Y., Xie, H., & Zhang, L. (2018). A new spectral-spatial sub-pixel mapping model for
906 remotely sensed hyperspectral imagery. IEEE Transactions on Geoscience and Remote Sensing, 56, 6763-6778.
907 Zhang, Y., Atkinson, P.M., Li, X., Ling, F., Wang, Q., & Du, Y. (2017). Learning-based spatial-temporal superresolution mapping of
908 forest cover with modis images. IEEE Transactions on Geoscience and Remote Sensing, 55, 600-614.
909 Zhong, Y., Wu, Y., Xu, X., & Zhang, L. (2015). An adaptive subpixel mapping method based on map model and class determination
910 strategy for hyperspectral remote sensing imagery. IEEE Transactions on Geoscience and Remote Sensing, 53, 1411-1426.
911